

## Research paper

## Automated toolpath design of 3D concrete printing structural components

Yefan Zhi <sup>a</sup>, Hua Chai <sup>a</sup>, Teng Teng <sup>a</sup>, Masoud Akbarzadeh <sup>a,b</sup>,\*<sup>a</sup> Polyhedral Structures Laboratory, Weitzman School of Design, University of Pennsylvania, Philadelphia, USA<sup>b</sup> General Robotic, Automation, Sensing and Perception (GRASP) Lab, School of Engineering and Applied Science, University of Pennsylvania, Philadelphia, USA

## ARTICLE INFO

## Keywords:

3D concrete printing  
Design automation  
Porous structure  
Buildability  
Path planning  
Continuous toolpath  
Surface reconstruction

## ABSTRACT

3D concrete printing (3DCP) structural components for construction assemblies are known for reduced material use and enhanced efficiency and design freedom. This article investigates the limitations in the geometrical and toolpath design of 3DCP structural components and presents an automated and comprehensive approach to their toolpath design and optimization. It exploits hierarchical geometric data structures and graph algorithms to achieve the following features: (1) By analyzing the overhang of toolpaths, the method offers quantitative criteria for determining the buildability of the components and predicting failure, thus assisting design decisions. (2) It provides toolpath offsetting and filleting methods that can enhance the dimensional accuracy of the print concerning layer line textures and overfills. (3) For branching and porous geometries, the method creates as-continuous-as-possible toolpaths with minimal stop-starts based on their topologies, thus reducing seam defects. (4) It converts the toolpath into efficient visualization meshes representing layer line textures and toolpath meshes compatible with finite elements analysis. The proposed method is implemented as a plug-in software within the environment of Grasshopper<sup>®</sup> for Rhino<sup>®</sup> to facilitate designers and engineers working with 3DCP. The effectiveness and versatility of the tool are demonstrated through the toolpath design and printing of four sets of examples. The tool reduces the number of toolpaths by 90% for a typical 80 mm nozzle and takes 0.21 s per meter of toolpath to slice, analyze overhang, generate continuous printing toolpaths, and visualize the print.

## 1. Introduction

## 1.1. 3D concrete printing structures

Since the early 2010s, the construction industry has been extensively exploring the application of 3D printing [1]. With concrete being the most broadly used material in building construction [2], 3D concrete printing (3DCP) construction has received wide attention. The benefits of 3DCP can be summarized in three main aspects.

- Firstly, by additively depositing material, 3DCP construction is free of formworks, potentially saving the material and labor costs required by using formwork in cast-in-place concrete construction, which comprise 35%–60% of the total cost [3,4].
- Secondly, additive manufacturing is known for its efficiency in material usage [5] and production time [6,7]. Owing to the low cost of concrete and the need to prepare formworks, cast-in-place concrete structures usually prefer designs that are simple in geometry, resulting in excessive material use [8]. The additive manufacturing nature of 3DCP allows more efficient use of material by accommodating optimized geometries. Meanwhile, by eliminating formworks and integrating automated processes, 3DCP can also reduce construction time [9,10].

- Lastly, 3DCP offers unprecedented freedom and flexibility in designing and constructing expressive, efficient, and functional structures. Equipped with 3DCP technology, designers can opt for free-form, expressive geometries that are otherwise difficult to realize with cast-in-place or manual construction practice [11–13]. Moreover, it allows unique variations in the geometries of the building elements, which would require unique molds in the cast-in-place paradigm [10]. Designers and engineers can also realize efficient 3DCP structures with optimized geometrical designs [14–16]. Examples also show that utilizing complex geometries, 3DCP structures can embed acoustic [17,18] and thermal [17,19] functions. The added functionality can also be locally controlled, resulting in functionally graded material for digital construction [20,21].

## 1.2. 3D concrete printing structural components

Large-scale 3DCP applied in building constructions can be divided into three types: (1) 3D printing structural components for discrete

\* Corresponding author at: Polyhedral Structures Laboratory, Weitzman School of Design, University of Pennsylvania, Philadelphia, USA.  
E-mail address: [masouda@design.upenn.edu](mailto:masouda@design.upenn.edu) (M. Akbarzadeh).

assembly; (2) 3D printing formwork for cast-in-place; and (3) on-site printing of an entire structure [22]. Our study focuses on 3DCP structural components for the following benefits:

- When structural components are fabricated individually, it is easier and cheaper for the motion system to have more spatial freedom, allowing free-form design of the components. Examples of in-situ printing are primarily vertical walls, without integration of performative structural geometry or other architectural functionalities [23]. Due to the separation of printing and assembly and the lowered cost of trial and error, discrete systems formed by 3DCP structural components can exhibit intricacies such as extreme overhangs and porous surfaces.
- The printing orientation can vary from component to component, utilizing the anisotropic nature of 3DCP objects [24–26]. Examples show that with tailored toolpaths, 3DCP structural components can forge optimized structures whose form follows the flow of forces [27,28].
- In discrete systems, different types of reinforcements can be introduced into 3DCP components for them to pick up tensile and flexural forces [29,30]. It improves the structural performance and unlocks more design possibilities to fully utilize the free-form buildability advantages of 3DCP on a large scale.
- As a prefabrication method, 3DCP structural components are typically fabricated in labs and factories. There is no need to transport and erect a gantry-like system on site, which requires considerable labor and energy and has to be relocated every time a building is finished [25]. Neither is the size of the building limited by the on-site motion platform(s). In venues where construction time is limited, or the surrounding environment (space, weather, social factors, etc.) does not allow the use of a gantry, discrete systems are easy to implement and reduce interference to the site.

To make full use of these advantages, we require that the 3DCP structural components are buildable, structurally efficient or functional, dimensionally accurate, with contact faces for assembly and reinforcement, and of adequate sizes. While architects and designers might be familiar with the design and form-finding of efficient and expressive forms as surface geometries, converting them into fabrication schemes meeting the above criteria is challenging. We summarize the current limitations and challenges of geometrical and toolpath design in the following four aspects:

1. **Buildability limitation.** It is hard to determine the buildability of a design. In other words, when a surface geometry is prepared, there are limited methods that can predict if it can be successfully printed without significantly deforming or collapsing [29], especially when the printing shapes are free-form [31]. While conventional layer-by-layer 3D printing with thermoplastic filaments utilizes support structures that are printed together with the main body and removed afterward, it is impractical to utilize such support structures in 3DCP for construction as concrete supports are hard to remove, creating considerable material and energy waste, and requiring additional post-processing work [32]. 3DCP structural components have to be self-supporting during the print, without extreme overhangs that induce the falling of the material or the collapsing of the print body. We refer to such components as buildable. While current studies use topological optimization methods to create buildable designs based on given boundary conditions [33–35], they do not contribute to understanding and optimizing existing designs without inducing drastic changes. The buildability limitation calls for both the criteria to determine the buildability of a design and methods to optimize it.





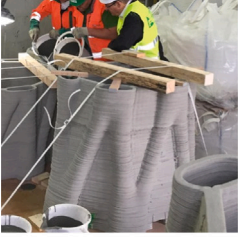







2. **Dimensional accuracy control.** For 3DCP structural components to effectively assemble structures, their dimensions must be accurate. Moreover, the contact faces between components need to be flat or interlocking. 3DCP systems typically use nozzles that are 10 to 50 mm wide and print layers at a thickness of 5 to 15 mm [25], resulting in visible layer lines and introducing a mismatch between the smooth surface design and the bumps [30,36–38]. While in fused filament fabrication (FFF), the surface of the prints can be polished to be smooth, in 3DCP, it is impractical and wasteful. In addition, the problem of deviation and over- and under-extrusion on a millimeter to centimeter scale substantially jeopardizes the surface quality [39–41]. For the 3DCP structural components to be accurate in dimension and comply with installation requirements, an automated optimization is needed for their toolpaths.
3. **Continuous printing.** Extrusion-based 3D printing favors continuous toolpaths over toolpaths with stop-starts in extrusion. Continuous toolpaths are free of non-extrusion travels, which may cause stringing issues, thus improving the surface quality [42,43]. As 3DCP consists of visually distinct layers printed with viscous concrete mortar, stop-starts in extrusion cause seam defects [36,44] and delamination, substantially affecting the surface quality of the print. However, current path-planning methods and software used in FFF rarely consider the continuity in toolpath as it is not a big problem for thermoplastics that extrude at a submillimeter scale [45]. Hergel et al. [46] presented a method for generating global continuous toolpaths for ceramic printing. However, it uses a considerable amount of material as support, which is not preferred in 3DCP. Zhong et al. [47] presented a method for creating as-continuous-as-possible toolpaths of surface models in ceramic printing, where larger overhangs are allowed compared with concrete. For designers of 3DCP structures, effectively making toolpaths continuous for intricate designs requires tailored algorithms and software.
4. **Visualization and simulation.** As layer lines of 3DCP objects are visually prominent, they must be incorporated into the design process. Once prepared, the toolpath curves can represent each print's fabrication scheme. However, an efficient visualization based on the toolpath curves is needed to fully display the aggregated texture of the concrete extrusion layers and utilize it for design iterations. Moreover, as designers and engineers navigate through different optimization options of a set of sliced toolpaths, the resulting structural performance also changes. To effectively assess the performance of the printing options, meshes representing the printed body that apply to finite element analysis (FEA) should be prepared [48,49]. As the toolpath curves might be modified during fabrication rationalization, the FEA-ready model should be based on the curves, not the initial surface geometry designed. The structural analysis calls for an efficient algorithm that generates such toolpath meshes based on toolpath curves.

Faced with the above limitations and challenges, an integrated approach to design the geometry and toolpath while maximizing the advantages of 3DCP would require tailored software and expertise in computing and processing geometries. However, such an integrated approach is only observed in a handful of studies, while half of the researchers conducted their toolpath design using slicing software designed for FFF. Most FFF toolpath generation studies cannot be borrowed for 3DCP due to the differences mentioned above [38].

### 1.3. Topology of the components

Table 1 shows a handful of 3DCP discrete structural assemblies that exploit free-form geometries for structural efficiency and formal expression. The components exhibit distinct geometrical features and

**Table 1**  
Structural systems built with 3DCP components, categorized according to the topological type of the units [50–55].

| Type           | Unit  | Assembly  | Source   |
|----------------|---|---|--|
| (a) Monolithic |    |    | Unreinforced masonry concrete bridge. Bhooshan [50].   |
| (b) Monolithic |    |    | Cable-supported concrete beam. Li et al. [51].   |
| (c) Monolithic |    |    | Truss-shaped concrete pillar (Supporting faces were cut to make the pieces porous). Gaudillière et al. [52]. |
| (d) Branching  |   |   | Post-tensioned concrete girder. Vantyghem et al. [53].   |
| (e) Branching  |  |  | Reinforced concrete tower. Anton et al. [54].  |
| (f) Porous     |  |  | Post-tensioned concrete canopy. Akbarzadeh et al. [55].  |

can be categorized according to their topologies. Topology analysis in 3D printing has been performed using medial axis [56,57] or Reeb graphs [58,59] for fabrication rationalization. Compared with other materials, 3DCP is primarily organized in horizontal planes with moderate overhang angles, making layer-based topology analysis similar to Reeb graphs a natural choice. Fig. 1 illustrates the three types of topology, showing color-coded visualizations and dependency graphs. Dependency graphs are made of vertices representing one-extrusion

patches and edges representing their dependency relations. The topology analysis method and the definition of dependency graphs will be further explained in Section 2.5.3. Here, we discuss the benefits and challenges of each type of component.

- A *monolithic* unit (Fig. 1a) is homeomorphic to a cylindrical extrusion (“Extrusion” here refers to the cylindrical surface geometry, not the material extrusion). Each layer is a closed curve, and



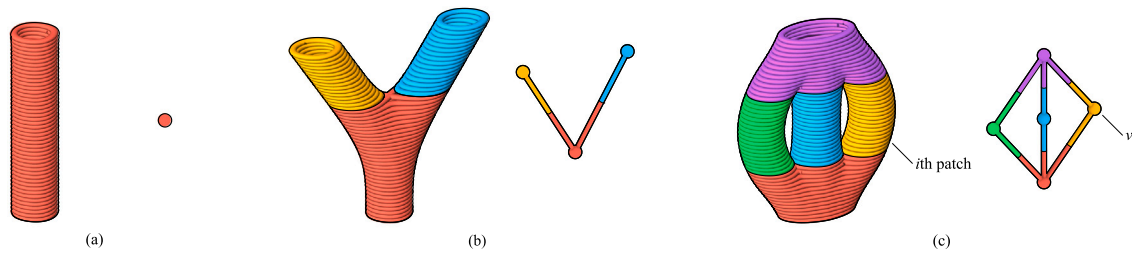


Fig. 1. Color-coded print visualizations and dependency graphs of three topological types of structural components: (a) monolithic; (b) branching; and (c) porous. (For interpretation of the references to color in this figure legend, the reader is referred to the web version of this article.)

by connecting adjacent layers, one toolpath can cover the entire geometry. It is widely used in 3DCP construction and extrusion-based printing of other viscous materials such as earth [60], clay [61], and biomaterials [62] where the target geometry is a simple, solid surface. Table 1a's cylindrical unit "folds" the planar closed curve of each layer into its walls to create infills. The component performs as having a multi-layer structure but remains a monolithic extrusion topologically for toolpathing convenience. In Table 1b, toolpath curves are post-processed to form created contact faces on the top and bottom. Table 1c is an example where the components are intended to be porous but are printed monolithically.

- A unit that is not monolithic involves multiple "islands" of closed curves in a single plane. They break the possibility of a globally continuous curve from the bottom to the top. The islands form multiple monolithic parts, with dependency relations observed and reflected in the dependency graphs.

- In a *branching* unit (Fig. 1b), the dependency graph is a tree without cycles. Table 1d and e are examples of efficient funicular structures made of branching units. The branching design helps the structures stay lightweight, without materials for the faces, as seen in Table 1c or Ooms et al. [63]. The toolpath generation methods are not disclosed in the two studies. If not aided by tailored algorithms and software, manually processing toolpaths to minimize the number of stop-starts can be tedious and time-consuming.

- A *porous* unit (Fig. 1c) may have branchings and mergings at the same time. Its dependency graph has cycles, necessitating a graph data structure. The toolpath design is more challenging than in branching units as the printing order of the islands has to meet dependency requirements.

Porous units have several additional benefits compared with branching units. Branching structures are prone to deformation due to vibration [64] or curing. Porous units have more geometrical constraints that help maintain dimensional accuracy during and after the printing. Porous units are also compatible with funicular structures across scales. If only monolithic or branching units are used, a structural system of multiple holes has to be segmented into small units at the sizes of the holes, adding to the time and labor cost of printing and handling. Using porous units, the segmentation design is free of this limitation and can adopt more economical sizes. Lastly, the design of porous assemblies and units can learn from the porous geometric prototypes that have been known to be structurally efficient, such as lattice structures [65] and minimal surfaces [66,67]. Table 1f is an example made of porous units based on the Diamond triply periodic minimal surface (TPMS). The geometry with a genus (number of holes) of 71 was segmented into 9 pieces with a single continuous contact surface between each pair of adjacent pieces. The toolpath generation and optimization of the porous pieces employed our proposed

method. If the units in Table 1c are sliced and printed using our method, the supporting faces can be removed or reduced, thus saving the material and post-processing effort while improving the consistency in the layer line texture. It is trivial that a method applicable to porous units would also accommodate monolithic or branching units.

#### 1.4. Scope of the study: Automated toolpath design

In light of the benefits of 3DCP structural components and the limitations restricting their geometric options, and in continuation with our past research in the 3DCP buildability and data structures [68,69], this study explores an integrated method of automated toolpath design. The study has three main objectives:

1. It identifies the limitations in the geometrical and toolpath design of 3DCP structural components. Based on that, it designs quantitative criteria for determining the buildability of the components and predicting failure.
2. It proposes a systematic approach to generate and represent the toolpaths for 3DCP structural components by slicing a surface input. The method utilizes a hierarchical geometric data structure based on carefully designed premises. Combining the data structure with graph algorithms, the method adapts to different types of geometries across materials and scales while leaving channels for manual modifications inside the integrated, automated system. It also rationalizes and optimizes the toolpaths for enhanced buildability, dimensional accuracy, and surface quality. Finally, it converts the toolpaths for continuous printing with minimal stop-starts.
3. It implements the method as a software plugin in Grasshopper® for Rhino®. Several examples are processed and printed to demonstrate the method's effectiveness and versatility. The limitations and opportunities for future development will be discussed.

"Toolpath generation" is often regarded as a separate step following the decision of the surface geometry in FFF and 3DCP construction. A designated toolpath generator and optimizer is "urgently needed for" 3DCP [38]. While this study aims to fill this gap between geometrical design research and toolpathing methods of 3DCP, it proposes an alternative phrase "toolpath design" for two reasons. Knowledge in toolpath generation and test results reflect the geometrical design by pointing out the limitations in buildability and suggesting possible improvements in the surface modeling and segmentation design of discrete systems. On the other hand, tailored adjustments to the toolpaths done by designers can improve the buildability and quality of the toolpaths, contributing to the design solution space.

The proposed method is automated and can produce desired toolpaths without additional manual input if the surface geometry is suitable. If the geometry has extreme features or requires specific handling, the integrated method also opens channels for the designer's input at every stage. The study hopes to liberate designers from the empirical



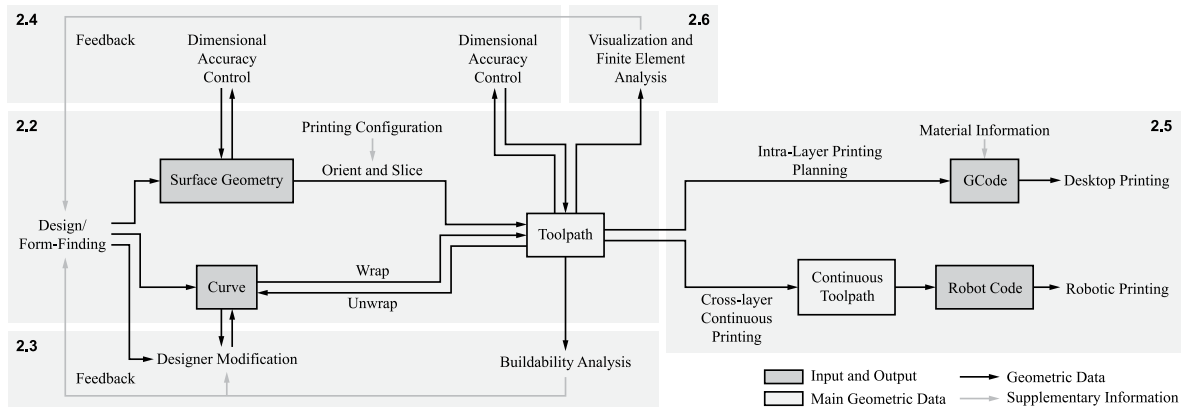


Fig. 2. Proposed toolpath design workflow. Numbers note respective sections in this article.

task of toolpath generation and equip them with automated and quantitative tools, thereby expanding and accelerating the research of 3DCP discrete structural systems.

## 2. Methodology

Section 2 is structured as follows. Section 2.1 introduces the proposed workflow of toolpath design. Several examples were designed to illustrate the subsequent methods. Section 2.2 introduces the orientation and slicing of the surface geometry, which is the groundwork of the proposed method. Sections 2.3 to 2.6 respond to the four limitations and challenges summarized in Section 1.2. Due to the length limitation, some parts of the proposed workflow are covered in the Supplementary Information (SI) and cited in the main text.

### 2.1. Toolpath design workflow

Fig. 2 gives a concise overview of the proposed toolpath design workflow. It primarily takes surface geometry as input. After slicing, the geometry is represented as toolpaths. Toolpaths are essentially parametric curves stored in a hierarchical data structure. The designer can modify these curves freely and then “wrap” them back as toolpaths. Or they can provide curves as input and wrap them as toolpaths (Section 2.2). Toolpaths can be converted into GCode for desktop gantry printers. In the case of 3DCP, toolpaths can be transformed into continuous toolpaths with minimal stop-starts and then converted to robot codes (Section 2.5). SI 1 introduces the setups compatible with the method and discusses its versatility across scales and materials. Utilizing the geometric data structure of toolpaths, designers can also assess the buildability of the component and modify it accordingly (Section 2.3), finetune the geometry to improve the dimensional accuracy and surface quality of the print (Section 2.4), and represent the result effectively for visualization and simulation purposes (Section 2.6).

To better illustrate the subsequent methods, four sets of examples are designed. Their printing results are visualized in Fig. 3. Fig. 3a is a brick system based on the porous modular facade “Design 1” by sculpturist Erwin Hauer in 1950 [70] (hereafter “Brick”). Fig. 3b is a Diamond TPMS geometry with a wavelength of 400 mm (hereafter “TPMS”). Fig. 3c is a discrete wall system with 6 components (hereafter “Wall”). The components are designed by morphing and trimming the Diamond TPMS unit. The contact faces between the vertically adjacent components are tilted. Fig. 3d is a porous panel “Design 6” by Erwin Hauer in 1956 [70] (hereafter “Panel”).

The main symbols used in the article are collected in Table 2.

### 2.2. Orientation and slicing

The slicing method lays the foundation of the workflow and is covered by the Supplementary Information. SI 2 discusses the nature of the slicing method and the requirement of the input surface geometry  $G$ . SI 3 provides a method to automatically orient the surface onto the printbed for slicing. SI 4 details the proposed parallel and rotary slicing methods using an input layer height  $t$ . The slicing result consists of  $n$  layers of toolpath curves. SI 5 discusses how the hierarchical toolpath data structure can also be obtained by wrapping existing curves, allowing custom modification to the toolpath. Finally, in SI 6, toolpaths curves are sorted into groups representing regions with consistent winding directions.

#### 2.2.1. Toolpath boolean operations

To effectively model and modify designs, designers often use the method of constructive solid geometry [71] where boolean operations are performed on multiple primitive solid objects to form a synthesis. For complex surface objects, the boolean operations can be buggy and time-consuming in practice. In preparing 3D printing toolpaths, the boolean operations can be instead performed on the toolpath curves after slicing the surface geometries separately using the same set of planes. As shown in Fig. 4, by having these planar curves sorted as regions with consistent winding directions, we can quickly form a directed graph representation and solve the result [72–74]. Fig. 5 shows an example of toolpath union where a TPMS-inspired geometry is reinforced at its branching and merging points by having more bridging layers. Surface union operation is challenging here due to inconsistent surface formats (mesh and non-uniform rational B-spline (NURBS) polysurface).

### 2.3. Cross-layer buildability

Researchers have utilized finite element models [48,49,75,76], mechanistic models [77], and lattice models [31,78] to predict the elastic buckling and plastic collapse failures in the printing and curing processes of 3DCP construction. However, most existing methods are limited to simple cylindrical forms and have not been tested with geometries of complex morphology and topology. The simulation methods also require substantial computation time, slowing design iterations.

#### 2.3.1. Overhang

To provide an agile tool for designers, we propose an alternative method of assessing the buildability of a design and predicting failures caused by extreme geometrical features. It analyzes the geometry’s overhang or how the toolpaths reach horizontally without support. Therefore, it does not rely on material information and applies to

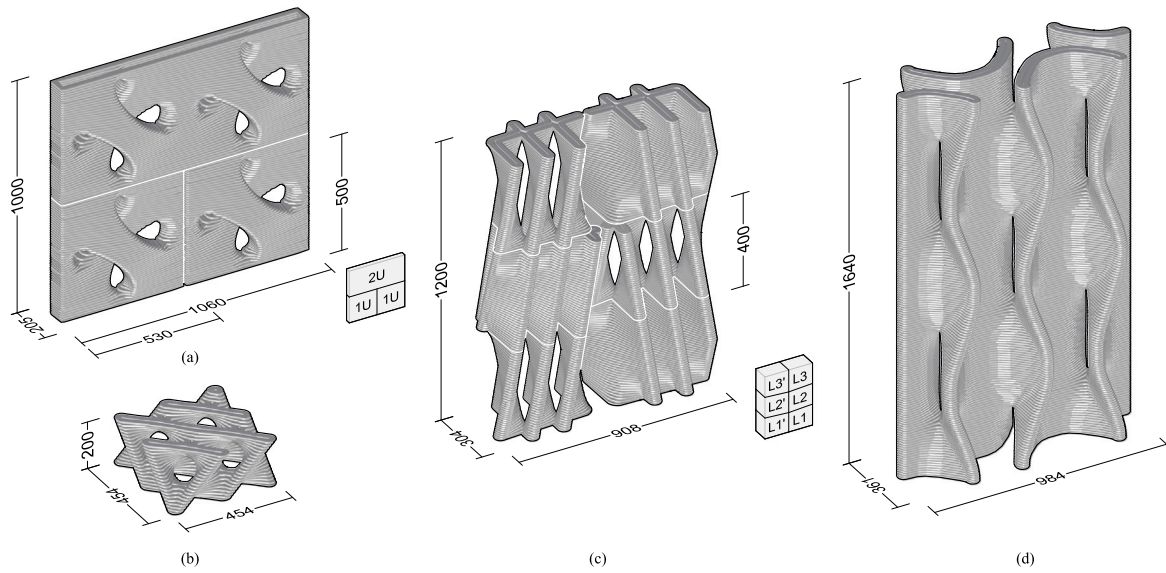


Fig. 3. Main examples used in this article, shown to a uniform scale: (a) “Brick”; (b) “TPMS”; (c) “Wall”; and (d) “Panel”. Units in mm.

Table 2

Nomenclature for the main symbols used in this article.

| Symbol                      | Description  | See           |
|-----------------------------|--|---------------|
| <b>Slicing</b>              |  |               |
| $G$                         | Input surface geometry   | SI 2          |
| $P_{\text{bottom}}$         | Bottom plane   | SI 3          |
| $P_{\text{bed}}$            | Printbed plane   | SI 3          |
| $\mathbf{n}_{\text{guide}}$ | Guide vector for the building direction  | SI 3          |
| $t_0$                       | Input layer height   | SI 4          |
| $n$                         | Number of layers   | SI 4          |
| <b>Extrusion</b>            |  |               |
| $t$                         | Actual layer height  | SI 4          |
| $t_d$                       | Local layer height at distance $d$ in rotary slicing                           | SI 4          |
| $w$                         | Extrusion width  | SI 4          |
| $r$                         | Sectional fillet radius  | Section 2.4   |
| <b>Buildability</b>         |  |               |
| $a$                         | Toolpath sample point distance   | Section 2.3.1 |
| $LOH_G$                     | Local overhang by ground   | Section 2.3.1 |
| $LOH_L$                     | Local overhang by layer  | Section 2.3.1 |
| $GOH$                       | Global overhang  | Section 2.3.1 |
| <b>Topology</b>             |  |               |
| $TP$                        | Toolpath   | Section 2.5.2 |
| $OETP$                      | One-extrusion toolpath   | Section 2.5.2 |
| $CTP$                       | Continuous toolpath  | Section 2.5.3 |
| $X_{i,j}$                   | The $j$ th curve of the $i$ th layer/patch in $X$ ( $TP$ , $OETP$ , or $CTP$ ) | Section 2.5.2 |
| $G_X$                       | Dependency graph of $X$ ( $TP$ , $OETP$ , or $CTP$ )                           | Section 2.5.2 |

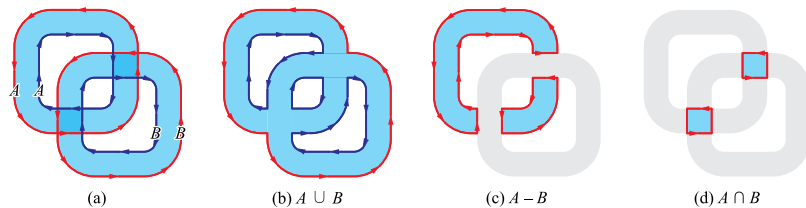


Fig. 4. Boolean operation of two sets of toolpaths, showing one layer: (a) input toolpaths  $A$  and  $B$ ; (b) union  $A \cup B$ ; (c) difference  $A - B$ ; and (d) intersection  $A \cap B$ .

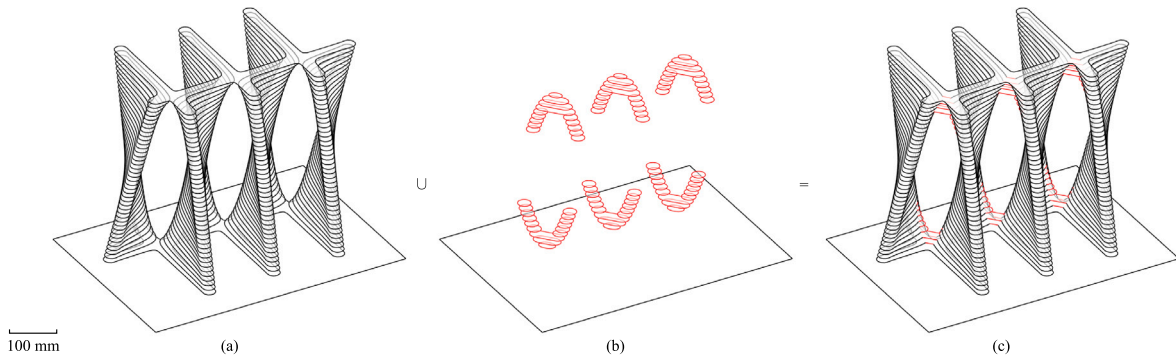


Fig. 5. Union operation of two sets of toolpaths (L2 of “Wall”): (a) primitive toolpaths found by slicing a mesh; (b) additional toolpaths found by slicing NURBS polysurfaces; and (c) unioned toolpath.

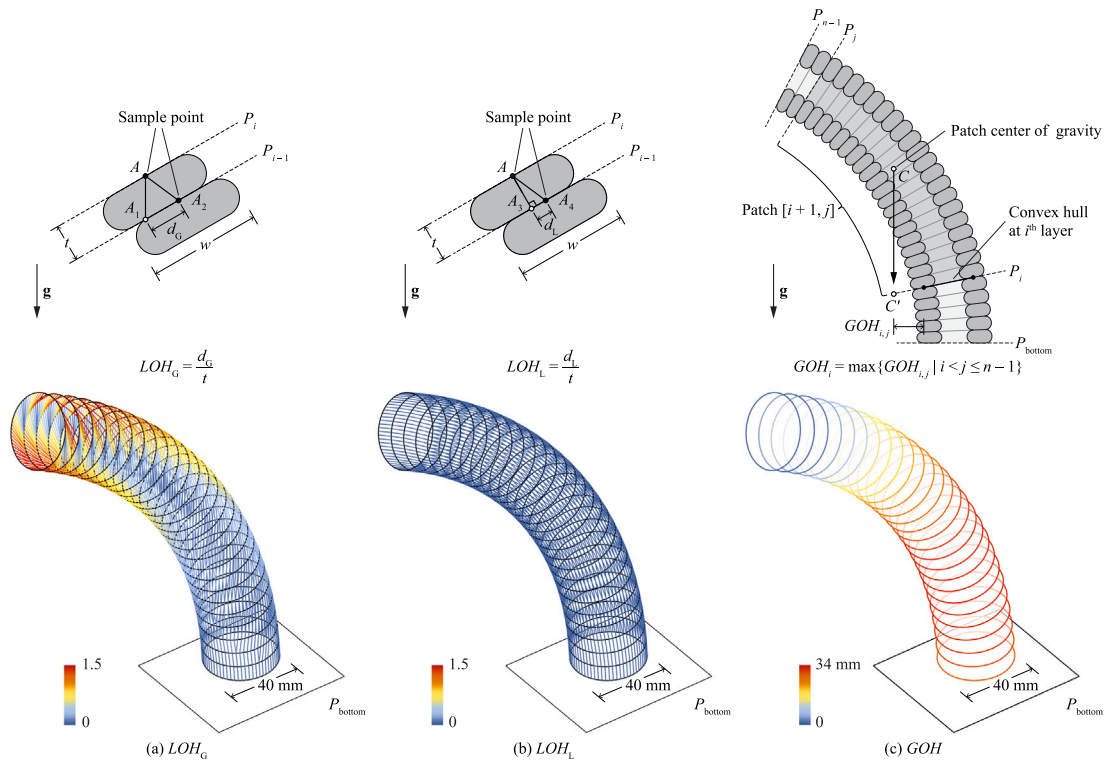


Fig. 6. The definitions and examples of: (a) local overhang by ground  $LOH_G$ ; (b) local overhang by layer  $LOH_L$ ; and (c) global overhang  $GOH$ . (For interpretation of the references to color in this figure legend, the reader is referred to the web version of this article.)

different setups of extrusion-based 3D printing. A monolithic example is designed by extruding a circle along an arc in Fig. 6 to illustrate the two types of overhang analysis:

- **Local Overhang (LOH).** Local overhang assesses how much support a small toolpath segment receives from the previous layer. The toolpaths are represented by sample points that divide toolpaths into segments of length  $a$ . (To balance the efficiency of computation and the accuracy of the analysis, we chose  $a$  to be around 1/5 of the layer thickness  $t$ , which upper bounds the change of overhang between adjacent sample points to 0.2. This number can be adjusted when needed.)  $LOH$  is a property of a sample point and has two types:

- *Local overhang by ground ( $LOH_G$ ).* As illustrated in Fig. 6a, a sample point  $A$  on  $P_i$  can be projected along the direction of gravity  $\mathbf{g}$  onto the previous plane  $P_{i-1}$  to get  $A_1$ .  $A_2$  is the sample point on  $P_{i-1}$  that is closest to  $A_1$ , seen as the support point for  $A$ . The local overhang by ground at  $A$  is

defined as

$$LOH_G = \frac{d_G}{t} = \frac{|A_1 A_2|}{t}.$$

If  $d_G$  is 0,  $A_2$  is precisely beneath  $A$ , making  $A$  fully supported. Fig. 6a is drawn using the plane defined by  $A$ ,  $A_1$  and  $A_2$ . However, the toolpath normals at  $A$  and  $A_2$  are not necessarily perpendicular to the plane. If the section is approximated as a rectangle with a width of  $w$ , then to have  $A_1$  touching the extrusion on  $P_{i-1}$  would require

$$d_G < \frac{w}{2} \quad \text{or} \quad LOH_G < \frac{w}{2t}$$

where the maximal  $LOH_G$  becomes 1.5 for a  $30 \times 10$  mm section. In practice, a buildable threshold for  $LOH_G$  is also material-dependent.

To visually inspect  $LOH$ , the lines between each sample point and its support point ( $AA_2$ ) are drawn and color-coded. In the example of Fig. 6a, the tip of the cylinder has extreme  $LOH_G$ .



- **Local overhang by layer ( $LOH_L$ )**. As illustrated in Fig. 6b, a sample point  $A$  on  $P_i$  can be oriented from  $P_i$  to the previous plane  $P_{i-1}$  to get  $A_3$ .  $A_4$  is the sample point on  $P_{i-1}$  that is closest to  $A_3$ , also seen as a support point for  $A$ . The local overhang by layer at  $A$  is defined as

$$LOH_L = \frac{d_L}{t} = \frac{|A_3A_4|}{t}.$$

$LOH_L$  measures the discontinuation of the toolpaths across adjacent layers. If we assume the material does not slump within the same layer and the friction between layers is sufficient, then  $LOH_L$  is a better criterion for determining buildability. In the example of Fig. 6b, the cylinder has consistent and very minimal  $LOH_L$ . The assumption behind  $LOH_L$  is closer to FFF using thermoplastics, while that of  $LOH_G$  is closer to 3DCP. The bent cylinder is challenging to print using concrete but is feasible using thermoplastics with a multi-axis printing system [79].  $LOH_G$  and  $LOH_L$  are the same in parallel slicing.

- **Global Overhang ( $GOH$ )**. The global overhang ( $GOH$ ) assesses if a patch of multiple layers is prone to collapse. It is a property of a toolpath curve. It can be solved after the toolpaths are organized as one-extrusion patches (detailed in Section 2.5.3). In a monolithic island of  $n$  layers where each layer is one curve, Fig. 6c illustrates the global overhang at the  $i$ th layer concerning the patch  $[i+1, j]$  ( $i < j \leq n-1$ ), denoted  $GOH_{i,j}$ . Patch  $[i+1, j]$  refers to the curves from the  $(i+1)$ th layer to the  $j$ th layer and is seen as a rigid body. Its center of gravity  $C$  can be projected along the direction of gravity  $\mathbf{g}$  onto  $P_i$  to get  $C'$ . If  $C'$  is inside the convex hull of the  $i$ th layer, the rigid body will not fall off its edge. Define  $GOH_{i,j}$  as 0. If  $C'$  is outside the convex hull, then  $GOH_{i,j}$  is the distance between them projected on the base  $xy$  plane. It is the moment arm of the rigid body's gravity concerning the edge of the convex hull. The global overhang of the  $i$ th layer is then calculated as

$$GOH_i = \max \{GOH_{i,j} | i < j \leq n-1\}.$$

In the example of Fig. 6c, the bottom layers have larger  $GOH$ , which means the cylinder is prone to break and fall at the bottom layers.

### 2.3.2. Overhang analysis

Overhang analysis can assist design decisions by suggesting whether a design is buildable and comparing multiple designs. Fig. 7 shows a comparative test of four types of TPMS (Gyroid, Schwartz P, Diamond, and Neovious). The  $LOH$  visualization (Fig. 7b) shows that the Diamond surface has floating islands without supports. It would require further trimming to be buildable. The  $GOH$  visualization (Fig. 7c) shows that both Gyroid and Diamond surfaces have legs prone to collapse. In contrast, the four bent walls of the Schwartz P surface tend to break at multiple locations. For direct comparison between the four types, the cumulative distribution function

$$y_{LOH}(x) = P(LOH \leq x) = \frac{\sum_{LOH_i \leq x} w_i}{\sum_i w_i}$$

is applied to represent each geometry as a curve (Fig. 7d), where  $LOH_i$  and  $w_i$  denote the  $i$ th sample point's  $LOH$  and weight (length of toolpath it represents). Any point  $(x, y)$  on the curve suggests that the proportion of toolpaths with  $LOH$  less than or equal to  $x$  is  $y$ . The higher the curve, the less overhang the geometry has. A line at  $x = 1$  is also drawn, showing our empirical threshold for buildable geometry. The result shows that compared with the other three, while the Neovious surface has fewer points with moderate overhangs ( $LOH \leq 1$ ), it has twice as many points with extreme overhangs ( $LOH > 1.25$ ) and is thus harder to print. While the other three types of TPMS have a

similar amount of extreme overhangs, Gyroid and Diamond surfaces have fewer points with moderate overhangs and are more buildable. In our software implementation, the analysis of each TPMS takes only 5 to 10 seconds on a laptop with Intel Core i9-13950HX CPU and 32 GB of RAM.

Overhang analysis can also be used to determine printing schemes. For example, Fig. 8 suggests that a porous unit of "Wall" has less local overhang in its original orientation ( $\mathbf{n}_{\text{guide}} = \mathbf{e}_z$ ) than in the flipped orientation ( $\mathbf{n}_{\text{guide}} = -\mathbf{e}_z$ ).

Fig. 9 shows how  $GOH$  analysis predicts printing failures. In a printing experiment of another unit of "Wall", islands collapsed at locations with extreme  $GOH$  (A and B). With the tool of local and global overhang analysis, designers can eliminate unbuildable design options without the effort of printing.

### 2.3.3. Overhang optimization

With quick overhang analysis, designers can adjust geometries respectively to enhance buildability. They can either modify the surface input  $G$  and reslice when substantial change is required or locally optimize the toolpath curves. The benefit of *local optimization* is that it targets curves of extreme overhangs without affecting the rest, causing minimal changes in the final print result.

Fig. 10 illustrates the local optimization using *overhang offset*.  $G$  (Fig. 10a) is an endpiece of the bridge in Table 1f. After slicing, the interior capping curves have extreme  $LOH$  (red in Fig. 10b). The new capping curves are generated by recursively offsetting the bottom curve by a desired overhang (1 in this example) and orienting it to the next plane. They exhibit consistent  $LOH$  (orange in Fig. 10c). The printing visualizations (introduced in Section 2.6) also suggest that the new capping curves are easier to print. Note that the optimization through the overhang offset process introduces a deviation from the initial design, and the number of layers might change. In Fig. 10, the capping curves are hidden after the discrete prints are assembled. In other cases, the designer must verify if the final model aligns with the design intent and input boundary conditions.

Another method of local overhang optimization is modeling additional geometries and then using *boolean operations* to update the toolpaths (similar to Fig. 5).

More generally, sliced toolpath curves can be modified locally and wrapped again (SI 5). A comprehensive discussion of the different scenarios of overhang optimization is beyond the scope of this article.

In addition to optimizing the overhang value of the sample points, adjusting the seam point of the close toolpath curves also increases the buildability. An example is provided in SI 7.

## 2.4. Dimensional accuracy control

This section discusses measures to accurately match the dimensions of the production and the design surface for assembly purposes. The sectional shape of material extrusion depends on various factors, including the nozzle size, layer height, extrusion speed, etc. [80]. Based on our experimental results and a review of existing literature [81,82], we propose a sectional model that is characterized by three parameters (Fig. 11a): layer width  $w$ , layer thickness  $t$  ( $t_d$  for rotary slicing), and fillet radius  $r \geq 0.5t$ . While in Fig. 11, the section is drawn as a smooth capsule shape with  $r = 0.5t$ , the following discussion also applies to  $r > 0.5t$ .

If the given surface  $G$  is the desired *boundary* of the print, it should not be sliced directly to form toolpaths. The center lines of the extrusion should sit *inside*  $G$  such that the sides of the extrusion will form  $G$ . Considering the bumps caused by  $r$ , the desired  $G$  should be tangent with the curved surfaces of the extrusion. Two primitive methods can be applied. In the *toolpath offsetting* method (Fig. 11b), the sliced curves of  $G$  are offset inward by  $0.5w$  on their respective planes (forming  $G_1$ ). However, the resulting sections protrude from  $G$ . In the *surface offsetting* method (Fig. 11c),  $G$  is offset inward by  $0.5w$  to get  $G_2$  and then sliced.

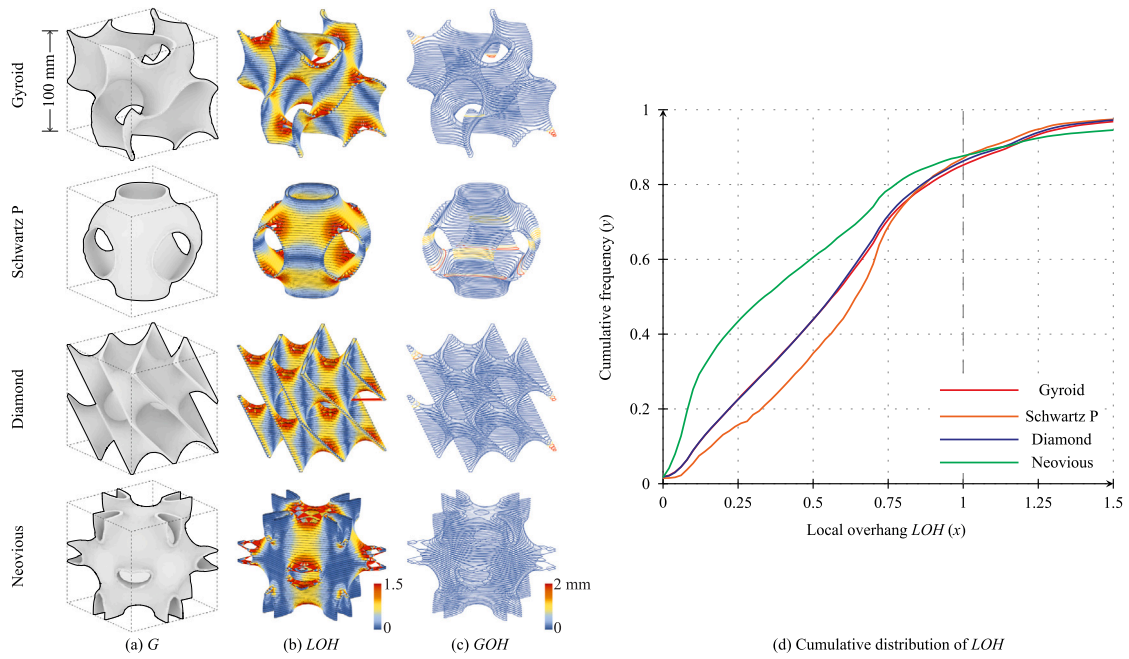


Fig. 7. Overhang analysis of double-sided TPMS units trimmed by a 100 mm cube. Units have a wavelength of 100 mm and a surface thickness of 3 mm. The layer thickness  $t = 2$  mm. (a) Input geometry  $G$ ; (b) local overhang  $LOH$ ; (c) global overhang  $GOH$ ; and (d) cumulative distribution of  $LOH$ .

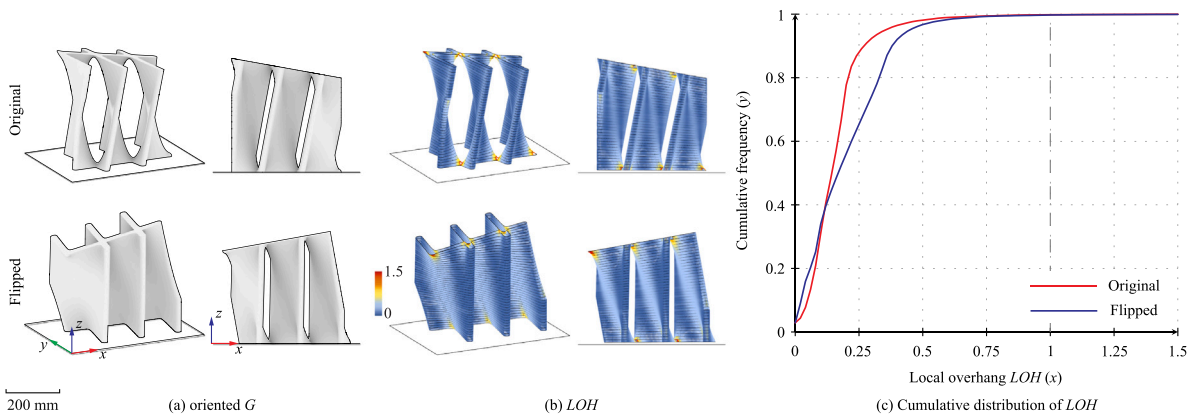


Fig. 8. Overhang analysis of the same  $G$  (a test version of L1 of “Wall”) oriented in two different ways: (a) oriented  $G$ ; (b) local overhang  $LOH$ ; and (c) cumulative distribution of  $LOH$ .

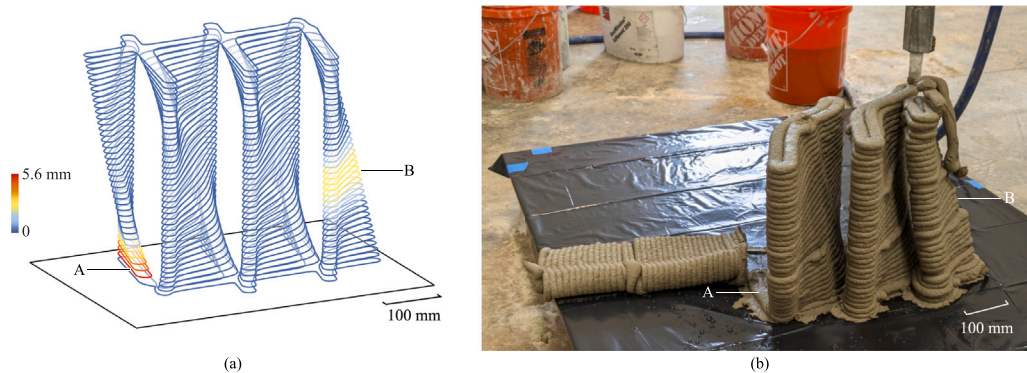


Fig. 9. A failed experiment on L2 of “Wall”: (a) breaks suggested by  $GOH$ ; and (b) result of the unfinished printing experiment.

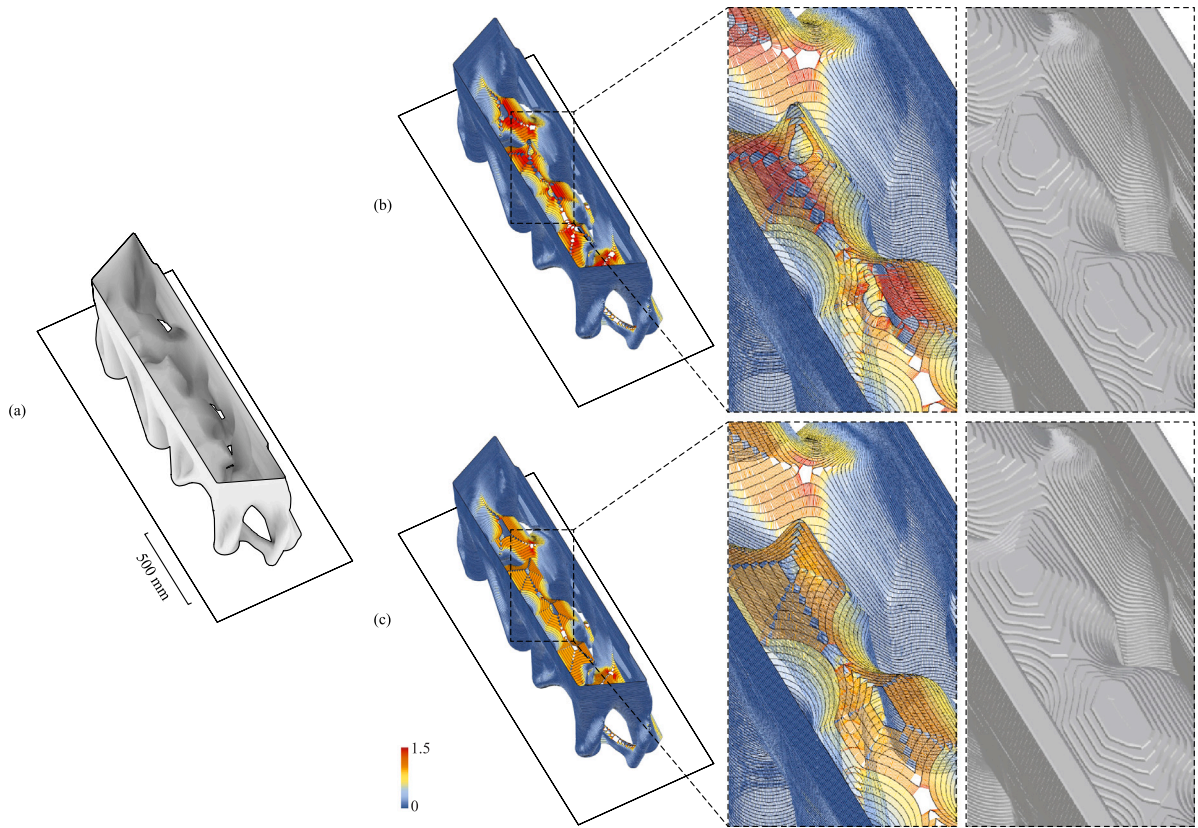


Fig. 10. Overhang optimization of capping curves through overhang offset, showing *LOH* visualization and printing visualization: (a)  $G$ ; (b) before optimization; (c) after optimization. (For interpretation of the references to color in this figure legend, the reader is referred to the web version of this article.)

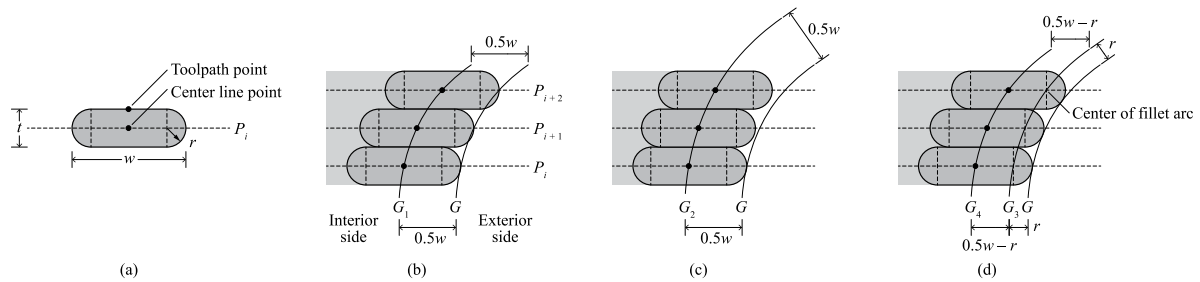


Fig. 11. Surface and toolpath offset settings for accurately matching the input  $G$  and printed layers: (a) sectional model of the extrusion; (b) toolpath offsetting method; (c) surface offsetting method; and (d) combined method.

The resulting sections, on the opposite, are kept inside  $G$  with a gap. To make the sectional arcs tangent to  $G$ , we propose a *combined method* (Fig. 11d).  $G$  is offset inward by  $r$  to get  $G_3$ , on which we expect to have the desired centers of the fillet arcs.  $G_3$  can be sliced, and the curves are then offset inward by  $0.5w - r$  on planes to get the final center lines of the extrusion (forming  $G_4$ ).

Surface offsetting of a solid surface can be done using the volumetric modeling method of signed distance functions. As the interior and exterior of  $G$  have different signs, we can easily offset a complex, porous  $G$  in a uniform direction.

To offset toolpaths in a uniform direction, we deal with solid regions that represent the volumes (SI 6) Since we orient the curves such that the left side is always inside the region (Fig. 12a), inward offsetting offsets curves to their left (Fig. 12b) while outward offsetting offset curves to their right (Fig. 12c). The local curve directions are preserved, while the number of curves and regions might change due to merging and splitting.

SI 8 discusses the measures to prevent overfills and deviation of extrusion at sharp corners to further improve the dimensional accuracy

of the production.

### 2.5. Continuous printing

This section introduces the intra- and cross-layer methods to make toolpaths as continuous as possible to decrease the number of stop-starts while preserving surface accuracy and quality.

#### 2.5.1. Intra-layer continuous printing

Fig. 13 illustrates how the number of toolpaths can be reduced in a layer organized as groups. *Simplify group* deals with each group of curves that form a region. It uses pairs of bridge lines to break and connect adjacent curves at the location where (i) they are closest to each other and (ii) the distance is under a designated threshold. In each region, the algorithm first traverses pairs of inner walls, searching for desired bridging locations. After the remaining inner walls cannot be further merged, the algorithm creates bridges between each inner wall and the outer wall if possible. This way, the number of visible



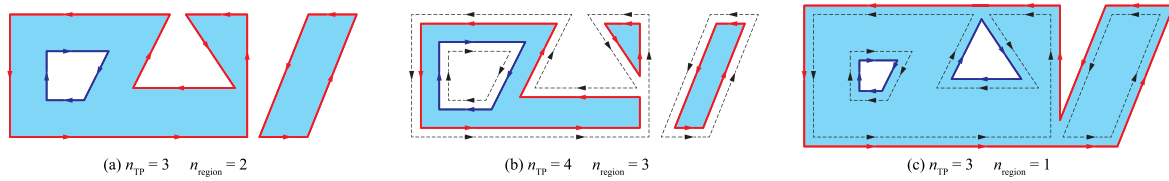


Fig. 12. Toolpath offsetting based on curve directions using linearized turns: (a) original toolpaths; (b) inward toolpath offsetting result; and (c) outward toolpath offsetting result.

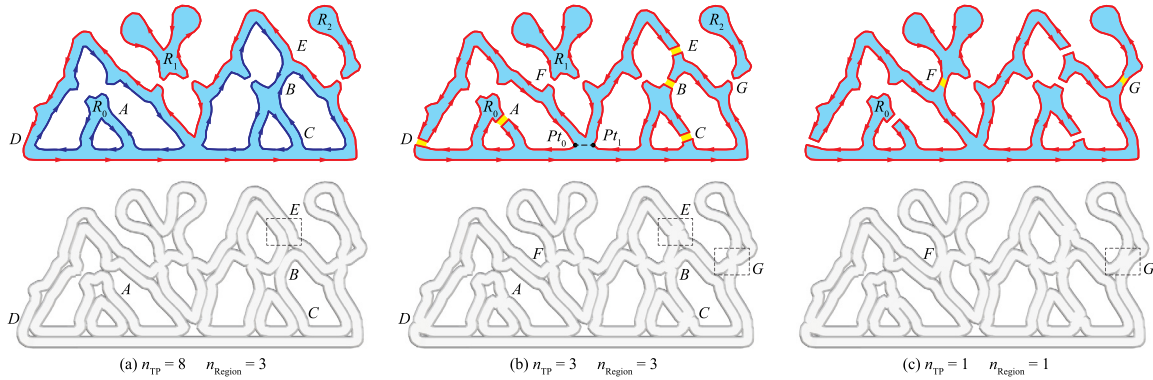


Fig. 13. Toolpath and visualization in intra-layer continuous printing: (a) a layer of original toolpath taken from a porous design; (b) result of simplifying groups; and (c) result of merging groups in (b). The effect of simplifying/merging is outlined at two locations. By having the distance between the parallel bridge lines smaller than the extrusion width  $w$ , the algorithm creates a slightly over-extruded area to ensure no void is left. The original void is preserved at other locations.

creases introduced on the outer wall is minimized. For example, group  $R_0$  in Fig. 13a has 5 inner walls, between which 3 pairs of bridge lines (A, B, and C in Fig. 13b) are created. The distance between  $P_{t_0}$  and  $P_{t_1}$  exceeds the merging threshold. Therefore, the two remaining inner walls must be merged with the outer wall using visible creases (D and E).

*Merge group* deals with pairs of groups close to each other. As shown by the visualization,  $R_0$  and  $R_1$ ,  $R_0$  and  $R_2$ , when printed, touch each other. The three groups can be merged by bridge lines at the touching locations to form one continuous outer wall (Fig. 13c). The visualizations show that the print result only has a minimal change in the process of reducing toolpath numbers. The order of the two operations can be reversed.

When a layer still has multiple toolpaths, the printing order of the toolpaths can be planned to minimize the travel length of the nozzle for a shorter printing time. Finding an optimal order with the shortest travel length is a variant of the metric traveling salesman problem (TSP), which is NP-hard [83]. Heuristic greedy algorithms such as the nearest neighbor [84] and the nearest insertion [85] can be used for quick optimization. (TSP is also seen in generating spacing filling curves [86], a different type of toolpaths in additive manufacturing.) However, if the next step is to create cross-layer continuous toolpaths, the in-plane order does not matter.

### 2.5.2. Cross-layer topology

This section introduces the algorithm to analyze the cross-layer topology of the print, as applied in Fig. 1. A simple, porous design is illustrated (Fig. 14a). Denote the hierarchical data structure of the sliced toolpaths organized in layers as  $TP$ . The  $j$ th curve of the  $i$ th layer is indexed as  $TP_{i,j}$  (Fig. 14b). In the alternative data structure of *one-extrusion toolpaths*, or *OETP*, the curves are divided into *one-extrusion patches* of cylindrical extrusions (Fig. 14c). Each patch is made of curves from different layers that form a continuous island when printed. For every pair of adjacent curves in a one-extrusion, the upper one is supported solely by the bottom one. The  $j$ th curve of the  $i$ th patch is indexed as  $OETP_{i,j}$ .

To organize the curves as *OETP*, we analyze the topological relationship between adjacent layers. This can be done using the definition

of  $LOH_L$  (Section 2.3.1). Each line in the wireframe model of  $LOH_L$  between  $P_{t_1} \in TP_{i,j}$  and  $P_{t_2} \in TP_{i+1,k}$  suggests that  $TP_{i+1,k}$  depends on  $TP_{i,j}$  (Fig. 14d). A directed *dependency graph*  $G_{TP}$  of  $TP$  can be formed such that each vertex represents a curve (Fig. 14e).  $G_{TP}$  has an edge  $(TP_{i,j}, TP_{i+1,k})$  if and only if there exist  $P_{t_1} \in TP_{i,j}$  and  $P_{t_2} \in TP_{i+1,k}$  such that  $P_{t_1}$  is sampled as  $P_{t_2}$ 's support point on the  $i$ th layer in the calculation of  $LOH_L$ .  $G_{TP}$  is very similar to the Reeb graph of  $G$  generated using a height function [87,88]. However,  $G_{TP}$  does not inspect the original surface continuation in  $G$ , and to reflect cross-layer supporting conditions, it should not.

$TP_{i,j}$  and  $TP_{i+1,k}$  belong to the same patch if  $TP_{i,j}$  supports only  $TP_{i+1,k}$ , and  $TP_{i+1,k}$  is supported only by  $TP_{i,j}$ . In other words,  $(TP_{i,j}, TP_{i+1,k})$  is the only outgoing edge of  $TP_{i,j}$  and the only incoming edge of  $TP_{i+1,k}$ . Based on this criterion, all curves can be organized into *OETP* utilizing the disjoint set data structure and a layer-by-layer searching algorithm (Fig. 14f).  $G_{TP}$  can be simplified as *OETP* dependency graph, or  $G_{OETP}$ , by merging the vertices in the same patch (Fig. 14g). Since all edges are from bottom layers to top layers, both  $G_{TP}$  and  $G_{OETP}$  are directed acyclic graphs (DAG).

### 2.5.3. Cross-layer continuous printing

To make toolpaths as continuous as possible, we first decide on the order of the curves utilizing the topology analysis such that more adjacent pairs of curves can be joined into one for fewer stop-starts. Our method is based on Zhong et al. [47] but uses a different greedy strategy that prioritizes the fabrication constraint.

A legitimate order requires that every curve be printed after its supporting curves, equivalent to the *topological sort* of the DAG  $G_{TP}$ . Printing the curves in layer ascending order (Fig. 14e 0 to 15) forms a legitimate topological sort. In the joining process to form  $G_{OETP}$ , the smallest index in each patch is kept (Fig. 14f 0, 2, 3, 4, 14). When simplified (Fig. 14g 0, 1, 2, 3, 4), they provide a topological sort of  $G_{OETP}$ .

However, another constraint not embedded in the graph representation is that as the nozzle travels, it should not collide with existing print. The nozzle and the extruding system have a complex shape. Computing its collision with all remaining curves every time a new curve is to be selected has a high time complexity. We adopt an estimation based

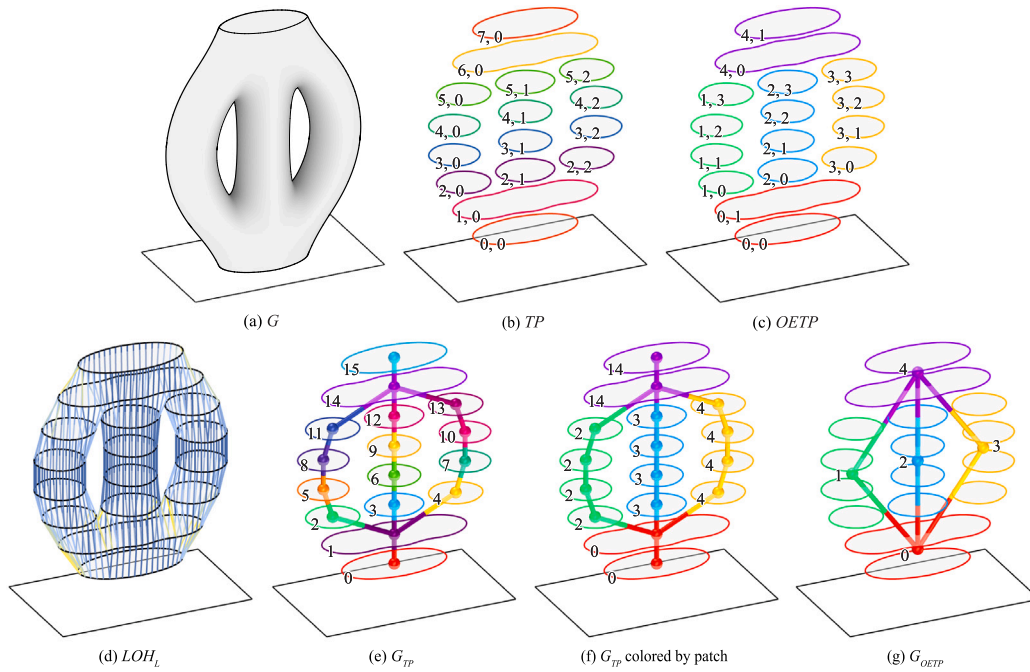


Fig. 14. Data structure and topology analysis of print. Input layer height  $l$  is exaggerated for display: (a) input geometry  $G$ ; (b)  $TP$  data structure; (c)  $OETP$  data structure; (d) wireframe model based on  $LOH_L$ ; (e)  $TP$  dependency graph  $G_{TP}$ ; (f)  $G_{TP}$  colored by patch; and (g)  $OETP$  dependency graph  $G_{OETP}$ . (For interpretation of the references to color in this figure legend, the reader is referred to the web version of this article.)

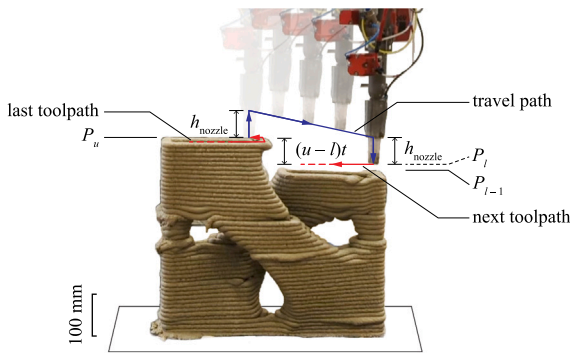


Fig. 15. Continuous printing under the constraint of the nozzle height  $h_{nozzle}$ .

on the height of the cylindrical nozzle  $h_{nozzle}$ . When the nozzle travels between toolpath curves. Say the lowest unprinted layer is the  $l$ th layer, and the highest printed layer is the  $u$ th layer. The nozzle need not go below the  $u$ th layer. Potential collision happens between layer  $u$  and  $l$ . We require that only the cylindrical part of the nozzle can potentially touch the printed layers (white in Fig. 15). This can be guaranteed only if

$$(u - l)t \leq h_{nozzle}.$$

Then

$$n_{gap} = \left\lfloor \frac{h_{nozzle}}{t} \right\rfloor$$

is the maximal layer index difference between the highest printed layer and the lowest unprinted layer. Based on this premise, travel paths can be created between consecutive toolpaths. Each travel path consists of three line segments: moving up by  $h_{nozzle}$ , moving to the next start point but leaving a  $h_{nozzle}$  vertical gap, and moving down by  $h_{nozzle}$  (Fig. 15). The vertical travels ensure that the nozzle does not collide with the existing print, whether the next toolpath is lower or higher than the previous one.

Under the dependency constraint and the layer difference constraint, we use a greedy algorithm to find an as-continuous-as-possible order (Algorithm 1). The output of the algorithm is the continuous toolpath  $CTP$ , a list of continuous patches. Each continuous patch is made of curves from consecutive layers that can be printed in one go.

As the algorithm proceeds, it maintains the set of candidate patches that satisfy the dependency constraint  $E$  and keeps track of the maximum allowed layer index  $u$  to limit the layer index difference. The greedy algorithm recursively looks for the next available one-extrusion patch in the following order of preference:

- Scenario 1. It can be merged with the previous continuous patch collected. The distance between the seam of the last curve in the previous continuous patch and the first curve in the chosen one-extrusion patch should be less than a designated tolerance  $d_{merge}$  such that a ramp can be created between the two curves for merging. (To avoid unsupported bridges, we used  $d_{merge} = 2t$ .) This means the two sub-patches of different one-extrusion patches can be merged into one continuous patch.
- Scenario 2. It has a max layer index no greater than  $u$ . We want to prioritize smaller patches that can be finished right away so that upcoming larger patches can potentially have fewer breaks.
- Scenario 3. It is closest to the seam point of the last curve in the previous continuous patch. This greedy strategy minimizes the travel length of the nozzle.

Each time the algorithm picks a one-extrusion patch, it might only take some of its lower layers to not exceed the maximal layer difference. As a result, some one-extrusion patches are subdivided. If the chosen continuous patch is going to be merged into the previous one, the seam point of its first curve is placed accordingly. Every continuous patch is a cylinder of curves that can be merged into one single cross-layer toolpath. The seam point of every planar curve is placed as close as possible to the previous curve in the cylinder (known as being “reseamed”).

Fig. 16a–f illustrates the greedy algorithm using a simple branching geometry. After the curves are reseamed and organized as  $CTP$ , they are connected using ramps. Every curve  $CTP_{i,j}$  is divided into two

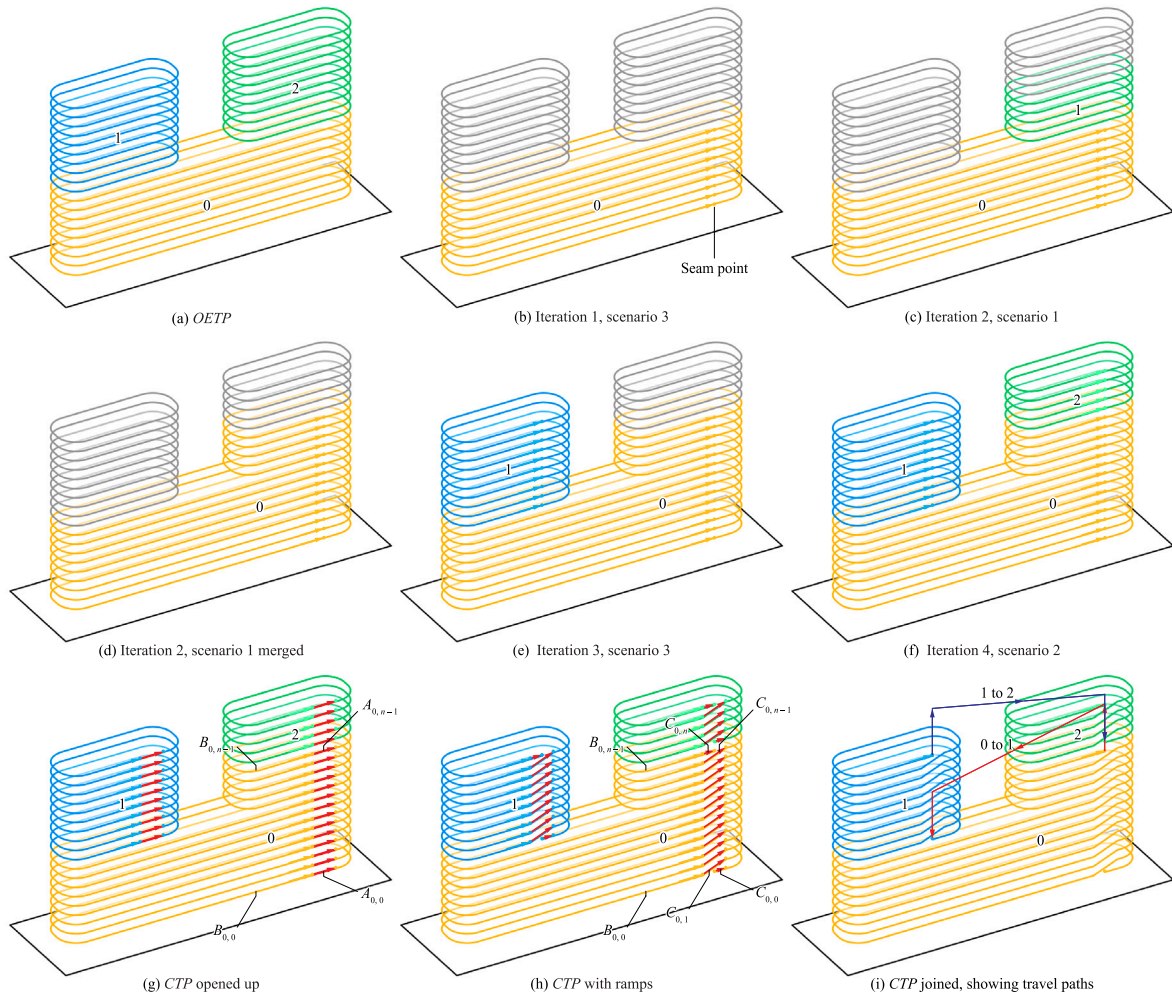


Fig. 16. Continuous printing planning and connecting with  $n_{gap} = 5$ : (a) input OETP; (b)–(f) continuous printing planning; and (g)–(i) continuous printing connecting.

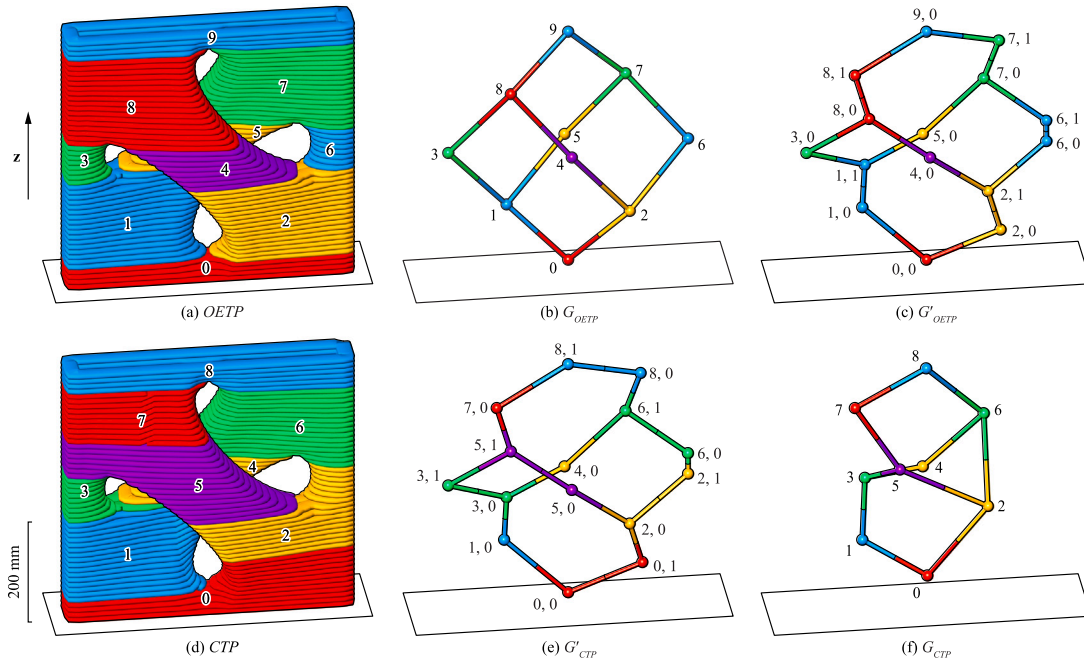


Fig. 17. Continuous printing planning of “Brick” using  $h_{nozzle} = 70$  mm: (a) visualization of OETP; (b)  $G_{OETP}$ ; (c)  $G'_{OETP}$  (subdivided  $G_{OETP}$ ); (d) visualization of CTP; (e)  $G'_{CTP}$  (subdivided  $G_{CTP}$ ); and (f)  $G_{CTP}$ . (For interpretation of the references to color in this figure legend, the reader is referred to the web version of this article.)



**Algorithm 1** CONTINUOUSPRINTINGPLANNING( $OETP, n_{\text{gap}}, d_{\text{merge}}$ )

---

**Input:**  
 $OETP$  — one-extrusion toolpath. Each patch  $E \in OETP$  is a list of curves and has:  
 $E.parent$  — set of patches that  $E$  depends on;  
 $E.child$  — set of patches that depends on  $E$ ;  
 $E.l$  and  $E.u$  — lower bound and upper bound of layer indices of curves in  $E$ ;  
 $E[i].seam$  — seam point of the  $i$ th curve  $E[i]$ ;  
 $n_{\text{gap}}$  — maximal layer index difference;  
 $d_{\text{merge}}$  — maximal distance for merging two patches.

**Output:**  
 $CTP$  — curves resealed and organized as continuous toolpath;

**Uses:**  
POINTCURVEDISTANCE( $Pt, Crv$ ) — returns the distance between  $Pt$  and its closest point on  $Crv$ ;  
POINTPOINTDISTANCE( $Pt_1, Pt_2$ ) — returns the distance between  $Pt_1$  and  $Pt_2$ ;  
RESEAM( $Crv, Pt$ ) — returns  $Crv$  with its seam point placed as close as possible to  $Pt$ .

```

1:  $CTP \leftarrow$  empty list
2:  $OETP_{\text{active}} \leftarrow \{E \in OETP \mid E.parent = \emptyset\}$ 
3: while  $OETP_{\text{active}} \neq \emptyset$  do
4:    $\triangleright$  Find the next one-extrusion patch  $E_{\text{next}}$ .
5:    $u \leftarrow \min \{E.l \mid E \in OETP_{\text{active}}\} + n_{\text{gap}}$ 
6:    $S \leftarrow \{E \in OETP_{\text{active}} \mid E.l \leq u\}$ 
7:    $merge \leftarrow$  False
8:   if  $CTP = \emptyset$  then
9:      $E_{\text{next}} \leftarrow (\arg \min_{E \in S} E.u)[0]$ 
10:  else
11:     $Pt_{\text{ref}} \leftarrow CTP[-1][-1].seam$ 
12:    if  $\exists E \in S, E.l = CTP[-1].u + 1$  and POINTCURVEDISTANCE( $Pt_{\text{ref}}, E[0]$ )
         $\leq d_{\text{merge}}$  then  $\triangleright$  Scenario 1.
13:       $E_{\text{next}} \leftarrow E$ 
14:       $E_{\text{next}}[0] \leftarrow$  RESEAM( $E_{\text{next}}[0], Pt_{\text{ref}}$ )
15:       $merge \leftarrow$  True
16:    else
17:      if  $\exists E \in S, E.u \leq u$  then  $\triangleright$  Scenario 2.
18:         $S \leftarrow \arg \min_{E \in S} E.u$ 
19:         $E_{\text{next}} \leftarrow (\arg \min_{E \in S} \text{POINTPOINTDISTANCE}(Pt_{\text{ref}}, E[0].seam)) [0]$ 
         $\triangleright$  Scenario 3.
20:   $\triangleright$  Solve the upper limit of the layer index in the next continuous
        toolpath  $u_{\text{next}}$ .
21:   $u_{\text{next}} \leftarrow \min \{E_{\text{next}}.u, \min \{E.l \mid E \in S, E \neq E_{\text{next}}\} + n_{\text{gap}}\}$ 
22:   $\triangleright$  Collect curves of the next continuous toolpath  $C_{\text{next}}$  and add to
         $CTP$ .
23:   $C_{\text{next}} \leftarrow E_{\text{next}} [ : u_{\text{next}} - E_{\text{next}}.l ]$ 
24:  for  $i \leftarrow 0$  to  $|C_{\text{next}}| - 2$  do
25:     $C_{\text{next}}[i + 1] \leftarrow$  RESEAM( $C_{\text{next}}[i + 1], C_{\text{next}}[i].seam$ )
26:  if  $merge$  then
27:     $CTP[-1] \leftarrow CTP[-1] + C_{\text{next}}$ 
28:  else
29:     $CTP.append(C_{\text{next}})$ 
30:   $CTP[-1].u \leftarrow u_{\text{next}}$ 
31:   $\triangleright$  Update information in  $OETP$ .
32:   $E_{\text{next}} \leftarrow E_{\text{next}} [u_{\text{next}} - E_{\text{next}}.l : ]$ 
33:   $E_{\text{next}}.l \leftarrow u_{\text{next}} + 1$ 
34:  if  $E_{\text{next}} =$  emptylist then
35:    for all  $E$  in  $E_{\text{next}}.child$  do
36:       $E.parent.remove(E_{\text{next}})$ 
37:      if  $E.parent = \emptyset$  then
38:         $OETP_{\text{active}}.add(E)$ 
39:     $OETP_{\text{active}}.remove(E_{\text{next}})$ 
40: return  $CTP$ 

```

---

segments:  $A_{i,j}$  of a fixed length  $L_{\text{ramp}}$  whose midpoint is the original seam, and  $B_{i,j}$ , the remainder (Fig. 16g). In the  $i$ th continuous patch of  $n$  curves, the  $j$ th cross-layer ramp  $C_{i,j}$  ( $j = 1, 2, \dots, n - 1$ ) is created by blending two adjacent layers as

$$c_{i,j}(t) = (1 - t)a_{i,j-1}(t) + ta_{i,j}(t), \quad 0 \leq t \leq 1$$

where  $a_{i,j}(t)$  represents  $A_{i,j}$  and  $t$  is the relative length parameter of  $a_{i,j}$  (Fig. 16h). Note that  $t$  is not necessarily the relative length parameter of the resulting  $c_{i,j}$ . Additionally,  $C_{i,0}$  is the second half of  $A_{i,0}$  and  $C_{i,n}$  is the first half of  $A_{i,n-1}$ . Then the  $i$ th single continuous toolpath curve is represented by the segments

$$C_{i,0}, B_{i,0}, C_{i,1}, B_{i,1}, \dots, C_{i,n-1}, B_{i,n-1}, C_{i,n}$$

to cover the entire cylinder in one go.

Similar to  $G_{TP}$  and  $G_{OETP}$ , we can represent the relations between continuous patches using a dependency graph  $G_{CTP}$ . Fig. 17 gives a graph-based view of how the curves are reorganized from  $OETP$  (Fig. 17a) to  $CTP$  (Fig. 17d) using a complex, porous example. In the process of the greedy search,  $G_{OETP}$ 's vertices representing the one-extrusion patches are subdivided such that a new DAG  $G'_{OETP}$  is formed (Fig. 17b, c).  $G'_{OETP}$  has two topological sorts, one following the original indices and one being the order of inquiry in the searching algorithm. The vertices can be reindexed according to the searching order, and adjacent vertices that will be merged will share the same color. This gives us a  $G'_{CTP}$  (Fig. 17e), identical to  $G'_{OETP}$  but with different indices and color codes. Finally, as determined by the search algorithm, the chosen vertices are merged to form  $G_{CTP}$  (Fig. 17f).

While our algorithm for continuous printing planning assumes the planar curves to be closed, they also assist the path planning of open curves. Huang et al. [89] summarized three cross-layer continuous printing scenarios: loop path (our method), retracing path, and alternate path. Our topology analysis and algorithm of organizing continuous patches also apply and are important to the last two scenarios with open curves, where simple post-processing would make each patch continuous.

A simple printing simulation can be performed to verify that the printing scheme is collision-free. If a collision is detected, the designer can opt for a smaller  $h_{\text{nozzle}}$  or manually modify the curves.

## 2.6. Visualization and simulation

SI 9 and 10 present the methods to generate efficient *visualization meshes* for representing the print and *toolpath meshes* for simulation. Fig. 18 shows how toolpath mesh assists the comparison between original toolpaths and optimized toolpaths. A volumetric modeling tool generates the input  $G$  (Fig. 18a). The optimized  $TP$  is prepared using the toolpath boolean method (Fig. 18b, Fig. 5). For both the original and optimized  $TP$ , three types of meshes are generated:

1. Toolpath mesh (Fig. 18c) is reconstructed using the discussed algorithm. The wireframe model captures the surface change caused by modifying the toolpath curves. However, this mesh is not ready for simulation as it does not consider the extrusion width.
2. Visualization mesh (Fig. 18d) is easy to generate and captures the difference. It is not simulation-ready since it has self-intersections and the interfaces between adjacent layers must be modeled separately.
3. *Thickened toolpath mesh* (Fig. 18e) is the toolpath mesh of the thickened toolpath. The thickened toolpath is the result of offsetting the toolpath by  $w/2$  on both sides (Section 2.4) and is not an actual "toolpath". The region they represent is the area filled with material extrusion. Therefore, the toolpath mesh of the thickened toolpath represents the volume of the print, as supported by a comparison between Fig. 18d and e. The thickened toolpath mesh is manifold, watertight, and free of self-intersection. With tools such as fTetWild [90], the surface meshes can be converted into volumetric meshes compatible with FEA software. Our FEA results (Fig. 18f) using Abaqus suggest that the optimized version has less maximal displacement under the load of 9 kN.

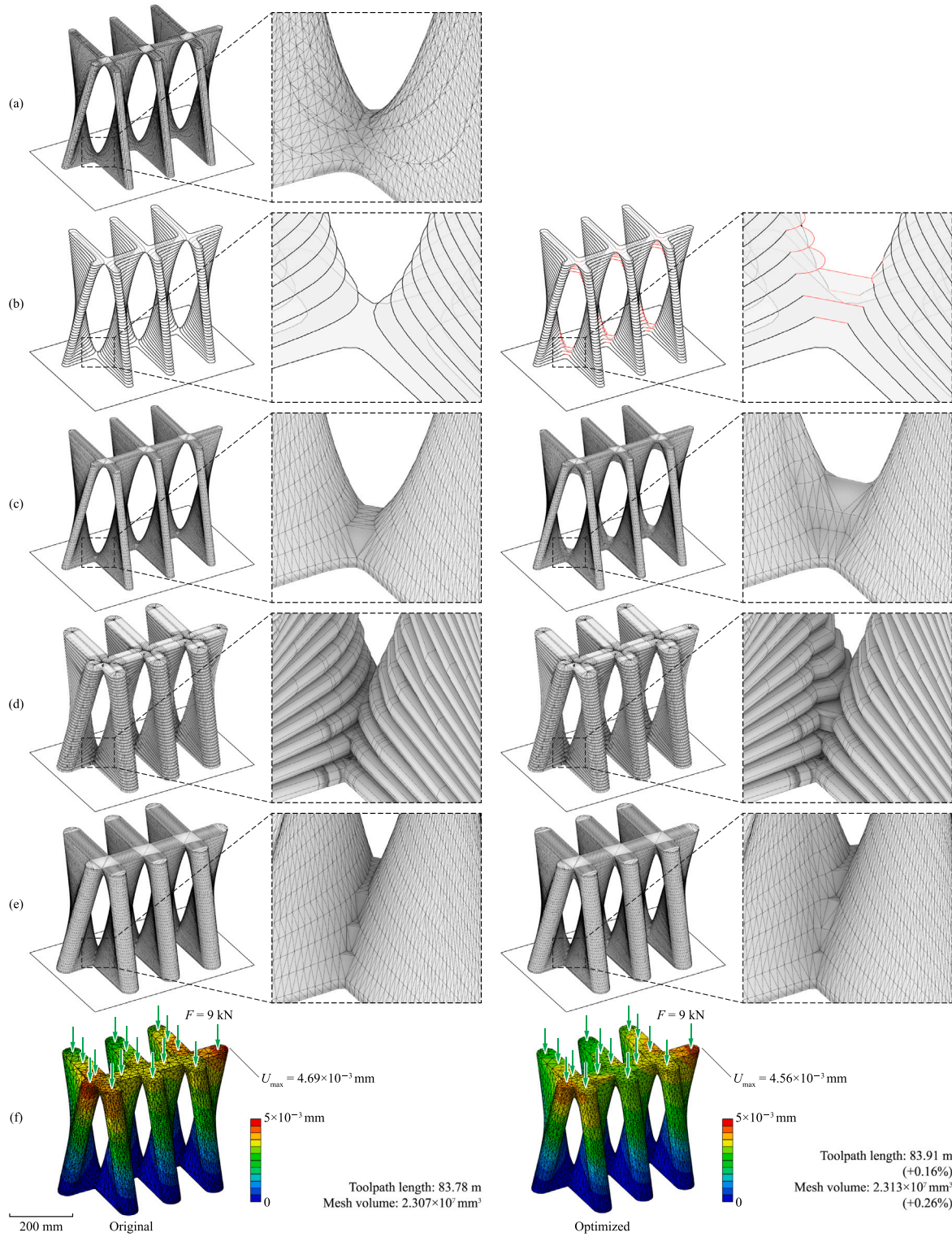


Fig. 18. Comparison between original and optimized toolpaths in Fig. 5, showing the mesh edges: (a) G; (b) TP; (c) toolpath mesh; (d) visualization mesh; (e) thickened toolpath mesh; and (f) FEA results showing the maximal displacements  $U_{\max}$ .

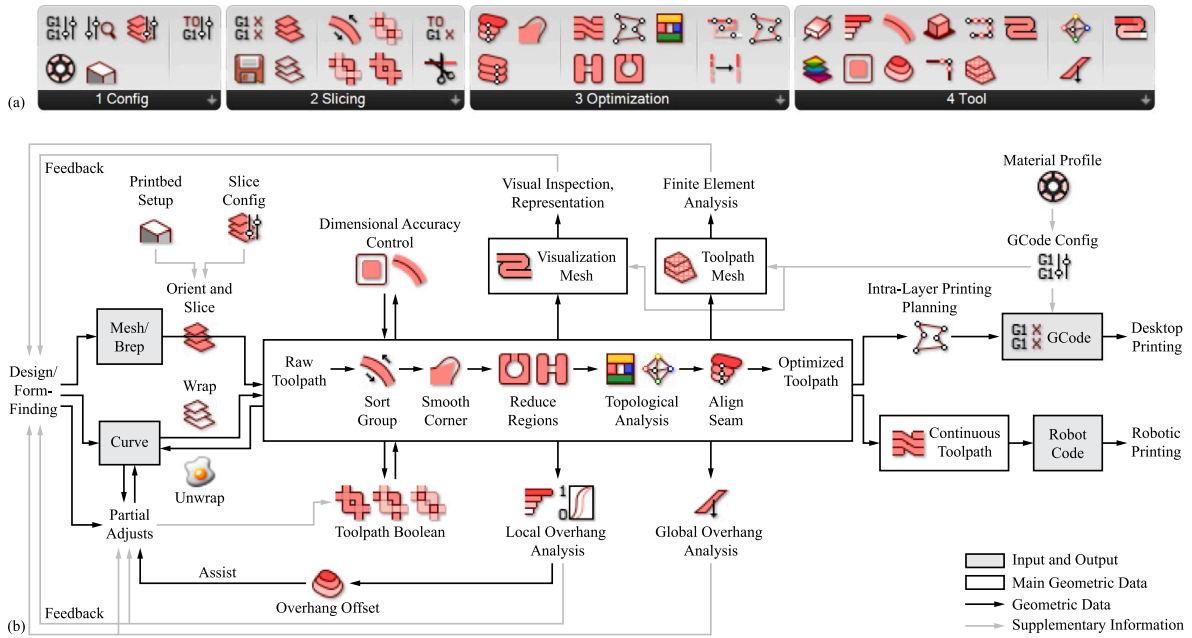


Fig. 19. Software implementation: (a) the component panel of Ovenbird for Grasshopper® and (b) the comprehensive workflow of using Ovenbird based on Fig. 2.

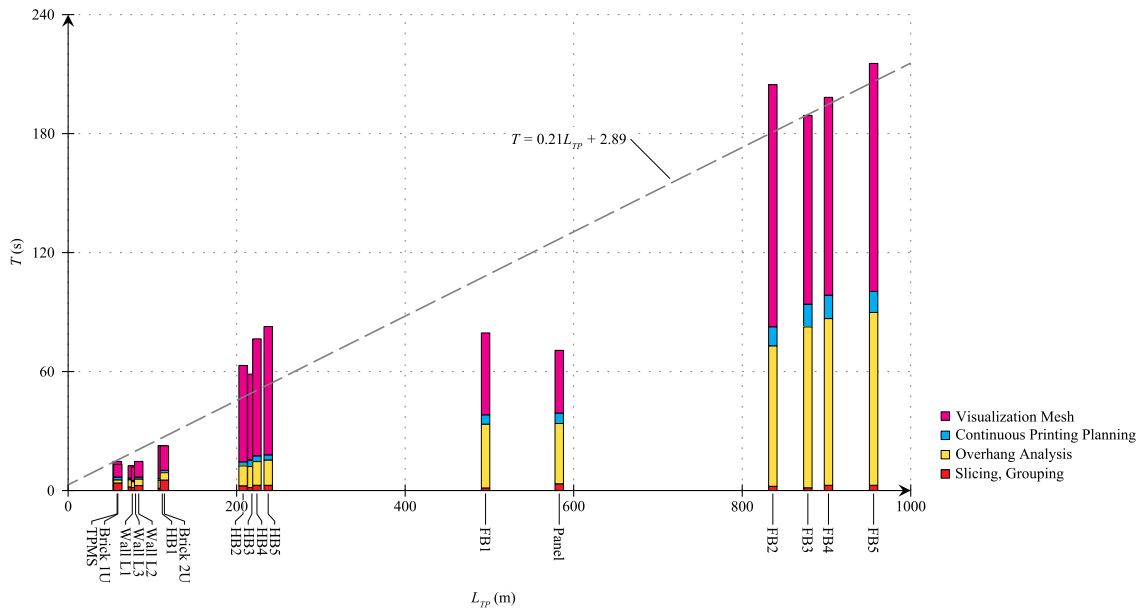


Fig. 20. Toolpath total length and computation time of different inputs.

### 3. Software implementation

We have implemented the discussed methods as a plug-in software named Ovenbird [91] within the modeling and visual programming environment Grasshopper® for Rhino®. The plug-in uses Grasshopper’s native methods and data types for handling and pipelining geometries, allowing users to intervene at any point (Fig. 19). The results and diagrams in this article are prepared using Grasshopper® and Ovenbird.

Fig. 20 shows the computation time of the examples concerning the total toolpath length. Tests were performed on a laptop with an Intel Core i9-13950HX CPU and 32 GB of RAM. The slicing and visualizing time needed for each component in this article is less than 2 min. Geometries from the half-scale bridge (HB1–5) and the full-scale bridge (FB1–5) in Table 1f are included to show large-scale applications. Linear regression shows that, on average, one meter of toolpath takes 0.21 s to compute and visualize.

### 4. Results

The proposed overhang analysis is performed on the sliced toolpaths of the four sets of examples. “Brick” and “TPMS” are optimized by modifying curves and rewrapping as toolpaths. The three “Wall” units are optimized using the toolpath boolean method. “Panel” is kept as sliced. Fig. 21 shows the local and global overhang of the optimized toolpaths and their visualization meshes.

The optimized toolpaths are then converted into continuous toolpaths through intra- and cross-layer continuous printing planning (Fig. 22). Table 3 compares the reduction in number of curves (or stop-starts) when  $h_{nozzle} = 80$  mm,  $t_0 = 10$  mm, and  $n_{gap} = 8$ , as used in our production.  $R_{subd} = n_{CTP}/n_{OETP}$  is the rate of subdivision of the one-extrusion patches. For smaller prints with  $R_{subd} < 1$ , the number of continuous toolpaths needed is less than the number of one-extrusion patches because of merging.  $p = (1 - n_{CTP}/n_{TP}) \times 100\%$  is the



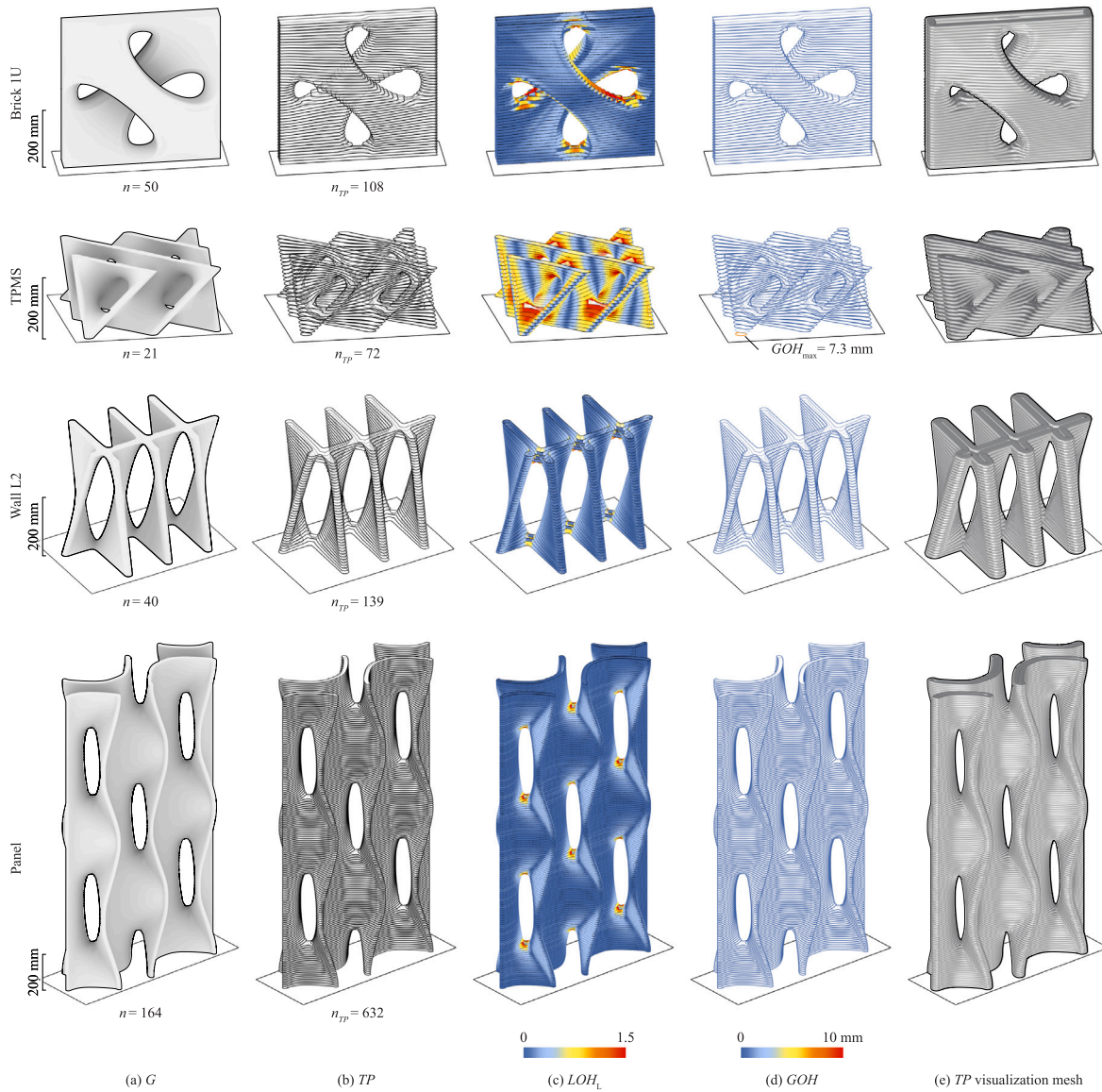


Fig. 21. Overhang analysis of the four examples: (a) *G*; (b) *TP*; (c) *LOH<sub>L</sub>*; (d) *GOH*; and (e) Visualization Mesh of *TP*.

**Table 3**  
Result of continuous printing planning.

| Design    | Unit | Bounding dimensions (mm) | <i>n</i> | <i>n<sub>TP</sub></i> | <i>n<sub>OETP</sub></i> | <i>n<sub>CTP</sub></i> | <i>R<sub>subd</sub></i> | <i>p</i> |
|-----------|------|--------------------------|----------|-----------------------|-------------------------|------------------------|-------------------------|----------|
| (a) Brick | 1U   | 530 × 205 × 500          | 50       | 108                   | 10                      | 8                      | 0.8                     | 92.6%    |
|           | 2U   | 1060 × 205 × 500         | 50       | 166                   | 15                      | 19                     | 1.3                     | 88.6%    |
| (a) TPMS  |      | 454 × 454 × 200          | 21       | 72                    | 16                      | 10                     | 0.6                     | 86.1%    |
| (c) Wall  | L1   | 439 × 254 × 452          | 39       | 103                   | 5                       | 9                      | 1.8                     | 91.3%    |
|           | L2   | 569 × 254 × 384          | 40       | 139                   | 6                       | 13                     | 2.2                     | 90.6%    |
|           | L3   | 554 × 254 × 457          | 41       | 109                   | 5                       | 9                      | 1.8                     | 91.7%    |
| (d) Panel |      | 984 × 361 × 1640         | 164      | 632                   | 24                      | 64                     | 2.7                     | 89.9%    |

percentage decrease in the number of curves to print. On average, the toolpaths experience a  $p = 90\%$  reduction in their numbers.

Different nozzle heights are tested in continuous printing planning to reveal their relationship with the number of *CTP*. Fig. 23 shows a roughly linear relationship between  $n_{\text{gap}}$  and  $n_{TP}/n_{CTP}$  that can be expressed as

$$\frac{n_{TP}}{n_{CTP}} \approx n_{\text{gap}} + 2$$

which gives us

$$p = \left(1 - \frac{n_{CTP}}{n_{TP}}\right) \times 100\% \approx \frac{n_{\text{gap}} + 1}{n_{\text{gap}} + 2} \times 100\%.$$

When  $n_{\text{gap}} = 8$ ,  $p \approx 90\%$ , in line with our results in Table 3.

Note that  $p \approx 50\%$  when  $n_{\text{gap}} = 0$ , because the planning algorithm creates ramps to connect certain pairs even if the nozzle height is set



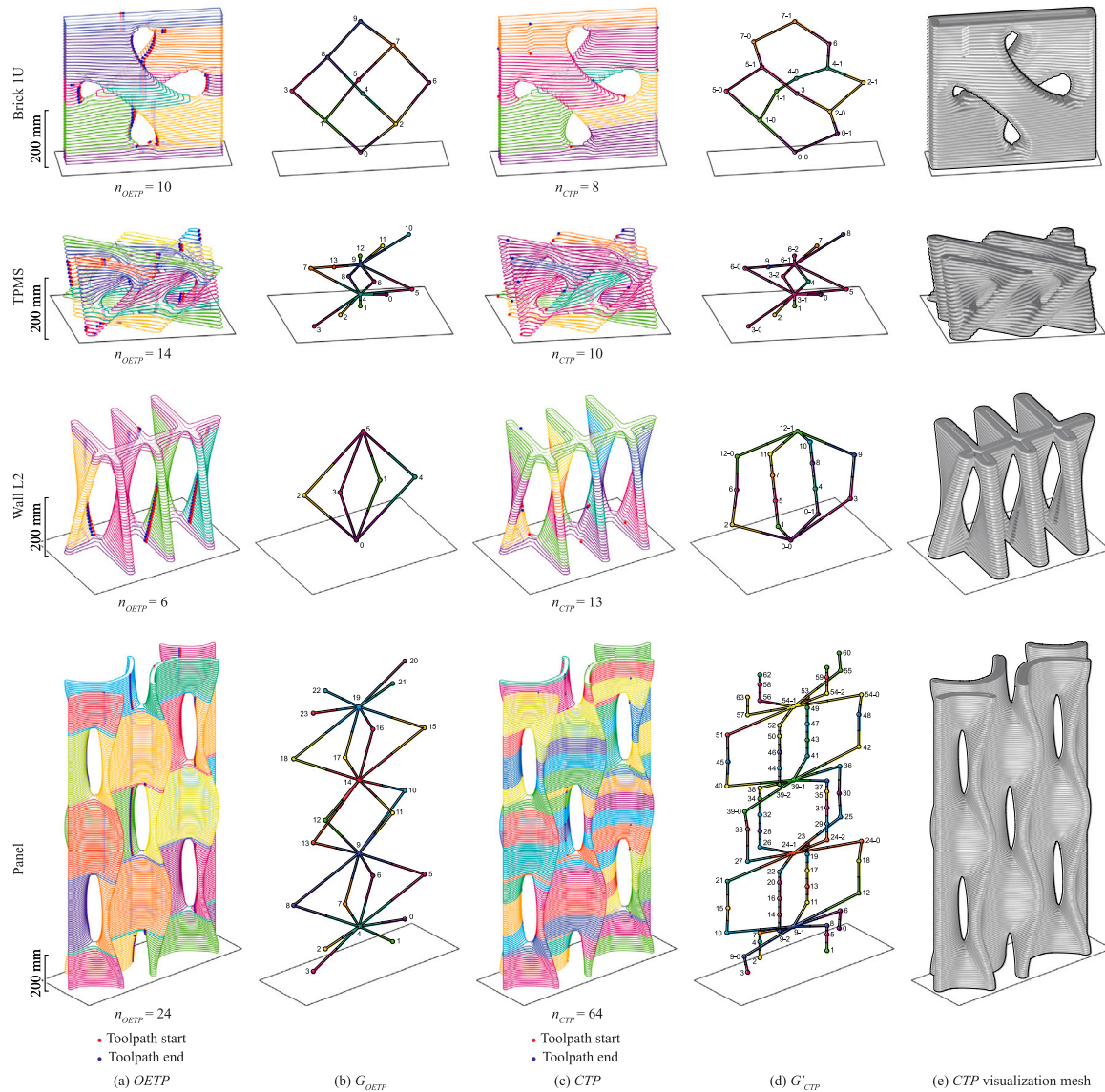


Fig. 22. Topological analysis and continuous printing planning of the four examples: (a)  $OETP$  (after intra-layer reducing); (b)  $G_{OETP}$ ; (c)  $CTP$ ; (d)  $G'_{CTP}$  (subdivided  $G_{CTP}$ ); and (e) visualization mesh of  $CTP$ , showing the ramps for connecting adjacent layers.

as 0. Thus, for thermoplastic printers where long nozzles are undesirable, the planning algorithm still significantly reduces the number of stop-starts.

There exist upper bounds for the reduction. The marginal utility becomes minimal as the nozzle height exceeds the average height of the one-extrusion patches ( $n_{gap} > n_{TP}/n_{OETP}$ , dashed in Fig. 23). To further illustrate this effect, scalded-up “TPMS” has been sliced and added to Fig. 23). Longer nozzles also bring a higher chance of collision, which is not considered in the greedy search.

All four sets of examples are successfully printed and assembled. The print result shows the effect of the distinct geometric features. Fig. 24a shows the slumping issue at the extreme overhangs ( $LOH \approx 1$ ) and bridges, while the islands build up without collapsing, as suggested by  $GOH = 0$ . Due to the small size of the islands, the bleeding seam defects inherent to the extruding system caused by the start-stops are also prominent. Fig. 24b shows that a single layer (half the wavelength) of Diamond TPMS surface can be thickened and printed. The overhang

analysis and the printing result suggest that for larger TPMS prototypes to be printed free of support, they have to be morphed and trimmed. The discrete wall system in Fig. 24c is an example of adapting TPMS prototypes and thus reducing local and global overhangs. The three bricks are segmented by single continuous faces with reinforced bridges for structural integrity. It shows the robustness of our method in dealing with non-planar geometries and building porous wall systems. Fig. 24d is a large panel unit that takes 70 min to print. The continuous printing planning minimized the number of start-stops to protect the layer line texture. While the porous panel was originally cast by the artist, our reproduction shows the advantage of additive manufacturing in rapid prototyping.

## 5. Conclusion

This article introduced an integrated, automated framework for toolpath design of 3DCP structural components. The framework is built

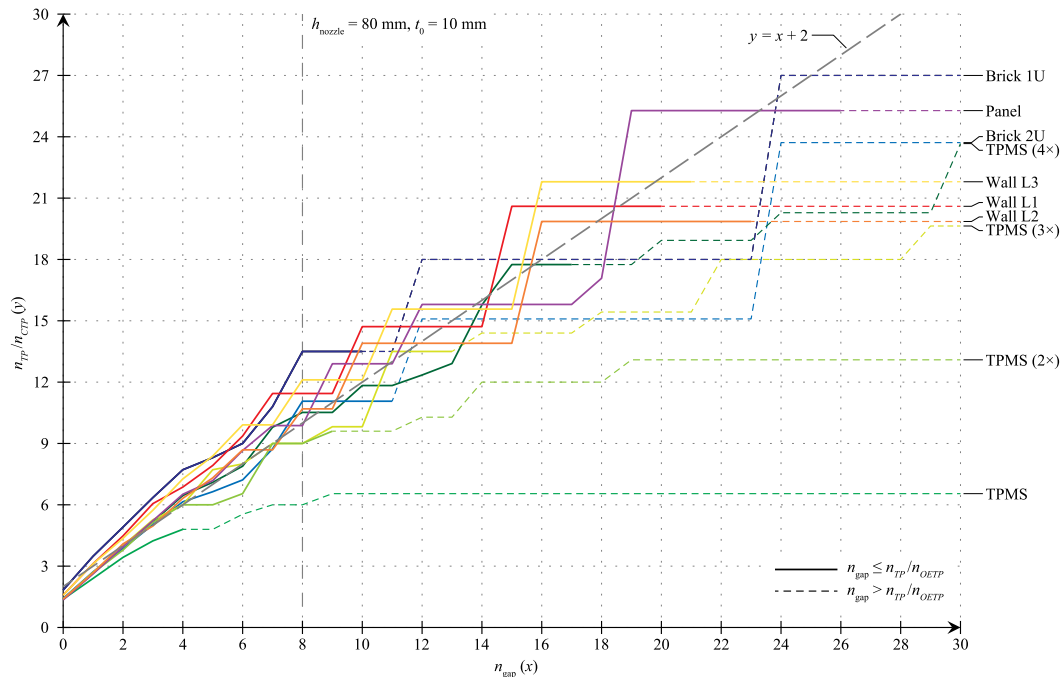


Fig. 23. Effect of nozzle height in continuous printing planning, seam not aligned.

upon a hierarchical data structure of sliced curves and is equipped with agile functionalities to assess and optimize the buildability of the geometry, enhance the dimensional accuracy of the print, create continuous toolpaths with minimized stop-starts for porous components and visualize the print and pipeline it for finite element simulation. It contributes to the knowledge of 3DCP design from geometrical perspectives by defining overhang properties, offering geometrical processing methods, and providing standards for utilizing meshes.

The robustness and efficiency of our software implementation and the underlying algorithms liberate designers from the tedious and empirical tasks of manual toolpath design and optimization. The effectiveness and versatility of the tool are demonstrated by four sets of examples and our previous research [55,92–94].

Currently, the method is limited in the following aspects. The toolpath-based overhang analysis does not take into account the rheology of the material or consider the speed and flow rate of the nozzle. For instance, a straight, thin wall is prone to buckling in reality but will be evaluated as buildable in our method. To better predict the buildability of the print, numerical analysis can be designed to incorporate these factors. The study can also be coupled with quantitative assessments of the dimensional accuracy of the final prints to increase the precision of the structural components for assembly. Planar printing with rotary slicing adapts to components with non-parallel faces. For certain free-form geometries, non-planar layers can improve the buildability. Alternative data structures and algorithms that accommodate non-planar layers and apply to the proposed analysis and optimization can be explored. For computation efficiency, the continuous printing planning algorithm relies solely on the nozzle height. An efficient searching algorithm that considers the nozzle-print collision can be further developed.

#### CRediT authorship contribution statement

**Yefan Zhi:** Writing – review & editing, Writing – original draft, Visualization, Software, Methodology, Investigation, Formal analysis, Data curation, Conceptualization. **Hua Chai:** Writing – original draft, Methodology, Formal analysis, Conceptualization. **Teng Teng:** Writing – original draft, Visualization, Resources, Methodology, Investigation, Data curation. **Masoud Akbarzadeh:** Writing – review & editing, Validation, Supervision, Resources, Project administration, Methodology, Funding acquisition, Conceptualization.

#### Declaration of competing interest

The authors declare that they have no known competing financial interests or personal relationships that could have appeared to influence the work reported in this paper.

#### Acknowledgments

The authors gratefully acknowledge the support provided by the Advanced Research Projects Agency – Energy (ARPA-E) Grant of the U.S. Department of Energy (DE-AR0001631), the National Science Foundation Future Eco Manufacturing Research Grant (NSF FMRG-CMMI 2037097), and the National Science Foundation CAREER Award (NSF CAREER-CMMI 1944691) awarded to Dr. Masoud Akbarzadeh. The authors thank Dr. Maximilian E. Ororbia, Pouria Vakhshouri, and Yi (Simone) Yang for their assistance in experiments.

#### Appendix A. Supplementary data

Supplementary material related to this article can be found online at <https://doi.org/10.1016/j.addma.2025.104662>.





Fig. 24. Print results: (a) “Brick”; (b) “TPMS”; (c) “Wall”; and (d) “Panel”.

## Data availability

Data will be made available on request.

## References

- [1] S. Hou, Z. Duan, J. Xiao, J. Ye, A review of 3D printed concrete: Performance requirements, testing measurements and mix design, *Constr. Build. Mater.* 273 (2021) 121745, <http://dx.doi.org/10.1016/j.conbuildmat.2020.121745>.
- [2] J. Gregory, H. AzariJafari, E. Vahidi, F. Guo, F.-J. Ulm, R. Kirchain, The role of concrete in life cycle greenhouse gas emissions of US buildings and pavements, *Proc. Natl. Acad. Sci.* 118 (37) (2021) e2021936118, <http://dx.doi.org/10.1073/pnas.2021936118>.
- [3] E.L. Kreiger, M.A. Kreiger, M.P. Case, Development of the construction processes for reinforced additively constructed concrete, *Addit. Manuf.* 28 (2019) <http://dx.doi.org/10.1016/j.addma.2019.02.015>.
- [4] Y.W.D. Tay, B. Panda, S.C. Paul, N.A.N. Mohamed, M.J. Tan, K.F. Leong, 3D printing trends in building and construction industry: a review, *Virtual Phys. Prototyp.* 12 (2017) <http://dx.doi.org/10.1080/17452759.2017.1326724>.
- [5] V.N. Nerella, V. Mechtcherine, Chapter 16 - studying the printability of fresh concrete for formwork-free concrete onsite 3D printing technology (CONPrint3D), in: J.G. Sanjayan, A. Nazari, B. Nematollahi (Eds.), *3D Concrete Printing Technology*, Butterworth-Heinemann, 2019, pp. 333–347, <http://dx.doi.org/10.1016/B978-0-12-815481-6.00016-6>.
- [6] P. Wu, J. Wang, X. Wang, A critical review of the use of 3-D printing in the construction industry, *Autom. Constr.* 68 (2016) <http://dx.doi.org/10.1016/j.autcon.2016.04.005>.



- [7] I. Kothman, N. Faber, How 3D printing technology changes the rules of the game, *J. Manuf. Technol. Manag.* 27 (2016) <http://dx.doi.org/10.1108/jmtm-01-2016-0010>.
- [8] F. Bos, R. Wolfs, Z. Ahmed, T. Salet, Additive manufacturing of concrete in construction: potentials and challenges of 3D concrete printing, *Virtual Phys. Prototyp.* 11 (3) (2016) 209–225, <http://dx.doi.org/10.1080/17452759.2016.1209867>.
- [9] S.C. Paul, G.P. van Zijl, M.J. Tan, I. Gibson, A review of 3D concrete printing systems and materials properties: current status and future research prospects, *Rapid Prototyp. J.* 24 (4) (2018) 784–798, <http://dx.doi.org/10.1108/RPJ-09-2016-0154>, Publisher: Emerald Publishing Limited.
- [10] R. van Woensel, T. van Oirschot, M. Burgmans, M. Mohammadi, K. Hermans, Printing architecture: An overview of existing and promising additive manufacturing methods and their application in the building industry, *Int. J. Constr. Environ.* 9 (2018) 57–81, <http://dx.doi.org/10.18848/2154-8587/CGP/v09i01/57-81>.
- [11] B. Khoshnevis, Automated construction by contour crafting—related robotics and information technologies, *Autom. Constr.* 13 (1) (2004) 5–19, <http://dx.doi.org/10.1016/j.autcon.2003.08.012>, The best of ISARC 2002.
- [12] R.A. Buswell, R. Soar, A. Gibb, A. Thorpe, The potential of freeform construction processes, in: 2005 International Solid Freeform Fabrication Symposium, The University of Texas at Austin, 2005, pp. 502–512, <http://dx.doi.org/10.26153/TSW/7107>.
- [13] A. Perrot, D. Rangeard, 3D printing with concrete: Impact and designs of structures, in: 3D Printing of Concrete, John Wiley & Sons, Ltd, 2019, pp. 125–144, <http://dx.doi.org/10.1002/9781119610755.ch5>.
- [14] K. Kinomura, S. Murata, Y. Yamamoto, H. Obi, A. Hata, Application of 3D printed segments designed by topology optimization analysis to a practical scale prestressed pedestrian bridge, in: F.P. Bos, S.S. Lucas, R.J. Wolfs, T.A. Salet (Eds.), *Second RILEM International Conference on Concrete and Digital Fabrication*, Springer International Publishing, Cham, 2020, pp. 658–668.
- [15] G. Hansemann, R. Schmid, C. Holzinger, J.P. Tapley, H.H. Kim, V. Sliskovic, B. Freytag, A. Trummer, S. Peters, Additive fabrication of concrete elements by robots: Lightweight concrete ceiling, in: *Fabricate 2020*, UCL PRESS, United Kingdom, 2020, pp. 124–129, *Fabricate 2020 : Making Resilient Architecture ; Conference date: 02-04-2020 Through 04-04-2020*.
- [16] C. Menna, L. Esposito, Flexural behaviour of steel-reinforced topology-optimised beams fabricated by 3D concrete printing, in: R. Buswell, A. Blanco, S. Cavalaro, P. Kinnell (Eds.), *Third RILEM International Conference on Concrete and Digital Fabrication*, Springer International Publishing, Cham, 2022, pp. 404–410.
- [17] L. Prasittisopin, K. Pongpaisanseree, P. Jiramaroatpong, C. Snguanat, Thermal and sound insulation of large-scale 3D extrusion printing wall panel, in: F.P. Bos, S.S. Lucas, R.J. Wolfs, T.A. Salet (Eds.), *Second RILEM International Conference on Concrete and Digital Fabrication*, Springer International Publishing, Cham, 2020, pp. 1174–1182.
- [18] C. Gosselin, R. Duballet, P. Roux, N. Gaudillière-Jami, J. Dirrenberger, P. Morel, Large-scale 3D printing of ultra-high performance concrete – a new processing route for architects and builders, *Mater. Des.* 100 (2016) <http://dx.doi.org/10.1016/j.matdes.2016.03.097>.
- [19] G. Dielemans, D. Briels, F. Jaugstetter, K. Henke, K. Dörfler, Additive manufacturing of thermally enhanced lightweight concrete wall elements with closed cellular structures, *J. Facade Des. Eng.* 9 (1) (2021) 59–72, <http://dx.doi.org/10.7480/jfde.2021.1.5418>.
- [20] T. Wangler, N. Roussel, F.P. Bos, T.A. Salet, R.J. Flatt, Digital concrete: A review, *Cem. Concr. Res.* 123 (2019) <http://dx.doi.org/10.1016/j.cemconres.2019.105780>.
- [21] A. Paolini, S. Kollmannsberger, E. Rank, Additive manufacturing in construction: A review on processes, applications, and digital planning methods, *Addit. Manuf.* 30 (2019) 100894, <http://dx.doi.org/10.1016/j.addma.2019.100894>.
- [22] J. Xiao, G. Ji, Y. Zhang, G. Ma, V. Mechtcherine, J. Pan, L. Wang, T. Ding, Z. Duan, S. Du, Large-scale 3D printing concrete technology: Current status and future opportunities, *Cem. Concr. Compos.* 122 (2021) 104115, <http://dx.doi.org/10.1016/j.cemconcomp.2021.104115>.
- [23] R. Buswell, W. Leal de Silva, S. Jones, J. Dirrenberger, 3D printing using concrete extrusion: A roadmap for research, *Cem. Concr. Res.* 112 (2018) 37–49, <http://dx.doi.org/10.1016/j.cemconres.2018.05.006>, SI : Digital concrete 2018.
- [24] G. Ma, Z. Li, L. Wang, F. Wang, J. Sanjayan, Mechanical anisotropy of aligned fiber reinforced composite for extrusion-based 3D printing, *Constr. Build. Mater.* 202 (2019) 770–783, <http://dx.doi.org/10.1016/j.conbuildmat.2019.01.008>.
- [25] J. Xiao, H. Liu, T. Ding, Finite element analysis on the anisotropic behavior of 3D printed concrete under compression and flexure, *Addit. Manuf.* 39 (2021) 101712, <http://dx.doi.org/10.1016/j.addma.2020.101712>.
- [26] B. Zahabizadeh, J.t.a. Pereira, C. Gonçalves, E.N.B. Pereira, V.M.C.F. Cunha, Influence of the printing direction and age on the mechanical properties of 3D printed concrete, *Mater. Struct.* 54 (2) (2021) 73, <http://dx.doi.org/10.1617/s11527-021-01660-7>.
- [27] L. Brescegello, R. Naboni, Toolpath-based design for 3D concrete printing of carbon-efficient architectural structures, *Addit. Manuf.* 56 (2022) 102872, <http://dx.doi.org/10.1016/j.addma.2022.102872>.
- [28] A. Dell'Endice, V. Bhooshan, H. Lombois-Burger, J. Megens, S. Bodea, H. Eiz, T. Chen, L. Regnault de la Mothe, S. Nana, S. Sanin, T. Bürgin, S. Bhooshan, T. Van Mele, P. Block, The phoenix bridge: Improving circularity of 3D-concrete-printed unreinforced masonry structures, in: *FABRICATE 2024*, UCL Press, Copenhagen, 2024, pp. 90–97.
- [29] B. Raphael, S. Senthilnathan, A. Patel, S. Bhat, A review of concrete 3D printed structural members, *Front. Built Environ.* 8 (2023) 1034020, <http://dx.doi.org/10.3389/fbuil.2022.1034020>.
- [30] B. Lu, Y. Weng, M. Li, Y. Qian, K.F. Leong, M.J. Tan, S. Qian, A systematical review of 3D printable cementitious materials, *Constr. Build. Mater.* 207 (2019) 477–490, <http://dx.doi.org/10.1016/j.conbuildmat.2019.02.144>.
- [31] Z. Chang, Y. Xu, Y. Chen, Y. Gan, E. Schlangen, B. Šavija, A discrete lattice model for assessment of buildability performance of 3D-printed concrete, *Comput.-Aided Civ. Infrastruct. Eng.* 36 (2021) <http://dx.doi.org/10.1111/mice.12700>.
- [32] K.V. Bhat, G. Capasso, S. Coniglio, J. Morlier, C. Gogu, On some applications of generalized geometric projection to optimal 3D printing, *Comput. Graph.* 102 (2022) 199–212, <http://dx.doi.org/10.1016/j.cag.2021.10.006>.
- [33] M. Bi, P. Tran, L. Xia, G. Ma, Y.M. Xie, Topology optimization for 3D concrete printing with various manufacturing constraints, *Addit. Manuf.* 57 (2022) 102982, <http://dx.doi.org/10.1016/j.addma.2022.102982>.
- [34] T. Zegard, G.H. Paulino, Bridging topology optimization and additive manufacturing, *Struct. Multidiscip. Optim.* 53 (1) (2015) 175–192, <http://dx.doi.org/10.1007/s00158-015-1274-4>.
- [35] A.T. Gaynor, J.K. Guest, Topology optimization considering overhang constraints: Eliminating sacrificial support material in additive manufacturing through design, *Struct. Multidiscip. Optim.* 54 (5) (2016) 1157–1172, <http://dx.doi.org/10.1007/s00158-016-1551-x>.
- [36] P. Nayyeri, K. Zareinia, H. Bougherara, Planar and nonplanar slicing algorithms for fused deposition modeling technology: a critical review, *Int. J. Adv. Manuf. Technol.* 119 (5) (2022) 2785–2810, <http://dx.doi.org/10.1007/s00170-021-08347-x>.
- [37] O. Bouzaglou, O. Golan, N. Lachman, Process design and parameters interaction in material extrusion 3D printing: A review, *Polymers* 15 (2023) <http://dx.doi.org/10.3390/polym15192289>.
- [38] X. Cao, S. Yu, H. Cui, Z. Li, 3D printing devices and reinforcing techniques for extruded cement-based materials: A review, *Buildings* 12 (4) (2022) <http://dx.doi.org/10.3390/buildings12040453>, URL: <https://www.mdpi.com/2075-5309/12/4/453>.
- [39] S. Sherugar, M. Birkett, M. Blacklock, Characterisation of print path deviation in material extrusion, *Prog. Addit. Manuf.* (2023) <http://dx.doi.org/10.1007/s40964-023-00502-y>.
- [40] Y. Huang, G. Fang, T. Zhang, C.C. Wang, Turning-angle optimized printing path of continuous carbon fiber for cellular structures, *Addit. Manuf.* 68 (2023) <http://dx.doi.org/10.1016/j.addma.2023.103501>.
- [41] Y. Huang, Y. Guo, R. Su, X. Han, J. Ding, T. Zhang, T. Liu, W. Wang, G. Fang, X. Song, E. Whiting, C. Wang, Learning based toolpath planner on diverse graphs for 3D printing, *ACM Trans. Graph.* 43 (2024) <http://dx.doi.org/10.1145/3687933>.
- [42] L. Xia, G. Ma, F. Wang, G. Bai, Y.M. Xie, W. Xu, J. Xiao, Globally continuous hybrid path for extrusion-based additive manufacturing, *Autom. Constr.* 137 (2022) 104175, <http://dx.doi.org/10.1016/j.autcon.2022.104175>.
- [43] M. Bi, L. Xia, P. Tran, Z. Li, Q. Wan, L. Wang, W. Shen, G. Ma, Y.M. Xie, Continuous contour-zigzag hybrid toolpath for large format additive manufacturing, *Addit. Manuf.* 55 (2022) 102822, <http://dx.doi.org/10.1016/j.addma.2022.102822>.
- [44] I.E. Yigit, I. Lazoglu, Helical slicing method for material extrusion-based robotic additive manufacturing, *Prog. Addit. Manuf.* 4 (2019) <http://dx.doi.org/10.1007/s40964-019-00090-w>.
- [45] Q. Wan, W. Yang, L. Wang, G. Ma, Global continuous path planning for 3D concrete printing multi-branched structure, *Addit. Manuf.* 71 (2023) 103581, <http://dx.doi.org/10.1016/j.addma.2023.103581>.
- [46] J. Hergel, K. Hinz, S. Lefebvre, B. Thomaszewski, Extrusion-based ceramics printing with strictly-continuous deposition, *ACM Trans. Graph.* 38 (2019) <http://dx.doi.org/10.1145/3355089.3356509>.
- [47] F. Zhong, Y. Xu, H. Zhao, L. Lu, As-continuous-as-possible extrusion-based fabrication of surface models, *ACM Trans. Graph.* 42 (3) (2023) <http://dx.doi.org/10.1145/3575859>.
- [48] V. Nguyen-Van, H. Nguyen-Xuan, B. Panda, P. Tran, 3D concrete printing modelling of thin-walled structures, *Structures* 39 (2022) <http://dx.doi.org/10.1016/j.istruc.2022.03.049>.
- [49] G. Vantygheem, T. Ooms, W.D. Corte, VoxelPrint: A grasshopper plug-in for voxel-based numerical simulation of concrete printing, *Autom. Constr.* 122 (2021) <http://dx.doi.org/10.1016/j.autcon.2020.103469>.
- [50] S. Bhooshan, *Shape Design of 3D-Concrete-Printed Masonry Structures* (Ph.D. thesis), ETH Zurich, 2022.
- [51] Y. Li, H. Wu, X. Xie, L. Zhang, P.F. Yuan, Y.M. Xie, FloatArch: A cable-supported, unreinforced, and re-assemblable 3D-printed concrete structure designed using multi-material topology optimization, *Addit. Manuf.* 81 (2024) 104012, <http://dx.doi.org/10.1016/j.addma.2024.104012>.

- [52] N. Gaudillière, R. Duballet, C. Bouyssou, A. Mallet, P. Roux, M. Zakeri, J. Dirrenberger, Large-scale additive manufacturing of ultra-high-performance concrete of integrated formwork for truss-shaped pillars, in: J. Willmann, P. Block, M. Hutter, K. Byrne, T. Schork (Eds.), *Robotic Fabrication in Architecture, Art and Design 2018*, Springer International Publishing, Cham, 2019, pp. 459–472.
- [53] G. Vantighem, W. De Corte, E. Shakour, O. Amir, 3D printing of a post-tensioned concrete girder designed by topology optimization, *Autom. Constr.* 112 (2020) 103084, <http://dx.doi.org/10.1016/j.autcon.2020.103084>.
- [54] A. Anton, C.W. Lin, E. Skevaki, M.-Y. Wang, T. Wangler, R.J. Flatt, A.G. Soto, L. Gebhard, W. Kaufmann, M. Hasmeyer, B. Dillenburger, Tor alva: A 3D concrete printed tower, in: *FABRICATE 2024: Creating Resourceful Futures, 2024*, pp. 252–259.
- [55] M. Akbarzadeh, H. Chai, Y. Zhi, M.E. Ororbia, T. Teng, M. Bernhard, D.M. Bolhassani, F. Yavartano, J. Tapia, K. Pajak, M. Bernard, L. Troussset, P. Kassabian, B. Waligun, Diamanti: 3D-printed, post-tensioned concrete canopy, in: *FABRICATE 2024: Creating Resourceful Futures, 2024*, pp. 292–301.
- [56] C. Wu, C. Dai, G. Fang, Y.-J. Liu, C.C. Wang, RoboFDM: A robotic system for support-free fabrication using FDM, in: 2017 IEEE International Conference on Robotics and Automation, ICRA, IEEE, 2017, <http://dx.doi.org/10.1109/icra.2017.7989140>.
- [57] X. Wei, S. Qiu, L. Zhu, R. Feng, Y. Tian, J. Xi, Y. Zheng, Toward support-free 3D printing: A skeletal approach for partitioning models, *IEEE Trans. Vis. Comput. Graphics* 24 (10) (2018) 2799–2812, <http://dx.doi.org/10.1109/TVCG.2017.2767047>.
- [58] J. Khatkar, L. Clemon, R. Fitch, R. Mettu, A reeb graph approach for faster 3D printing, in: 2022 IEEE 18th International Conference on Automation Science and Engineering, CASE, IEEE, 2022, <http://dx.doi.org/10.1109/case49997.2022.9926485>.
- [59] D.P.V.J. Jayakody, T.Y. Lau, H. Kim, K. Tang, L.E. Thomas-Seale, Topological awareness towards collision-free multi-axis curved layer additive manufacturing, *Addit. Manuf.* 88 (2024) <http://dx.doi.org/10.1016/j.addma.2024.104247>.
- [60] A. Curth, E.G. Alvarez, K. Feickert, C. Mueller, D.M. Schulte, M. Ismail, Sueños con tierra/concreto: Multi-material fabrication for low-carbon construction – an optimised floor system for affordable housing in Mexico, in: *FABRICATE 2024: Creating Resourceful Futures, 2024*, pp. 214–221.
- [61] B. Peters, F. Gramazio, M. Kohler, S. Langenberg, Building bytes: 3D-printed bricks, in: *Fabricate 2014: Negotiating Design & Making*, DGO - Digital original, UCL Press, 2017, pp. 112–119, URL:.
- [62] N. Diniz, F. Melendez, Living systems thinking and making: 3D printing with mycelium and upcycled waste materials, in: 110th ACSA Annual Meeting Proceedings, ACSA, Virtual, 2022, pp. 285–289, <http://dx.doi.org/10.35483/ACSA.AM.110.39>.
- [63] T. Ooms, G. Vantighem, Y. Tao, M. Bekaert, G. De Schutter, K. Van Tittelboom, W. De Corte, The production of a topology-optimized 3D-printed concrete bridge, in: R. Buswell, A. Blanco, S. Cavalario, P. Kinnell (Eds.), *Third RILEM International Conference on Concrete and Digital Fabrication*, Springer International Publishing, Cham, 2022, pp. 37–42.
- [64] H.-m. Zhao, Y. He, J.-z. Fu, J.-j. Qiu, Inclined layer printing for fused deposition modeling without assisted supporting structure, *Robot. Comput.-Integr. Manuf.* 51 (2018) 1–13, <http://dx.doi.org/10.1016/j.rcim.2017.11.011>.
- [65] Y. Wu, J. Fang, C. Wu, C. Li, G. Sun, Q. Li, Additively manufactured materials and structures: A state-of-the-art review on their mechanical characteristics and energy absorption, *Int. J. Mech. Sci.* (2023).
- [66] P. Liu, L. Lu, J. Liu, Path-driven shell lattices designed for continuous fiber composite 3D printing, *Addit. Manuf.* 78 (2023) 103838, <http://dx.doi.org/10.1016/j.addma.2023.103838>.
- [67] X. Guo, X. Li, E. Wang, J.Y. Fuh, W.F. Lu, W. Zhai, Bioinspired hierarchical diamond triply periodic minimal surface lattices with high energy absorption and damage tolerance, *Addit. Manuf.* 76 (2023) 103792, <http://dx.doi.org/10.1016/j.addma.2023.103792>.
- [68] Y. Zhi, H. Chai, T. Teng, M. Akbarzadeh, Local optimization of self-supporting shell structures in 3D printing: a skeleton method, in: *Proceedings of IASS 2023 Symposium Integration of Design and Fabrication*, Melbourne, Australia, 2023, pp. 171–181.
- [69] Y. Zhi, T. Teng, M. Akbarzadeh, Designing 3D-printed concrete structures with scaled fabrication models, *Archit. Intell.* 3 (1) (2024) <http://dx.doi.org/10.1007/s44223-024-00070-3>.
- [70] E. Hauer, Erwin hauer: continua, architectural screens and walls, Erwin Hauer: Continua, Architectural Screens and Walls, Princeton Architectural Press, New York, 2004.
- [71] A.A.G. Requicha, H.B. Voelcker, *Constructive Solid Geometry*, Technical Memorandum, number 25, Production Automation Project, University of Rochester, 1977.
- [72] K. Weiler, P. Atherton, Hidden surface removal using polygon area sorting, in: *Proceedings of the 4th Annual Conference on Computer Graphics and Interactive Techniques*, ACM, 1977, <http://dx.doi.org/10.1145/563858.563896>.
- [73] K. Weiler, Polygon comparison using a graph representation, *ACM SIGGRAPH Comput. Graph.* 14 (1980) <http://dx.doi.org/10.1145/965105.807462>.
- [74] Y.-X. Gong, Y. Liu, L. Wu, Y.-B. Xie, Boolean operations on conic polygons, *J. Comput. Sci. Tech.* 24 (2009) <http://dx.doi.org/10.1007/s11390-009-9246-z>.
- [75] R.J.M. Wolfs, A.S.J. Suiker, Structural failure during extrusion-based 3D printing processes, *Int. J. Adv. Manuf. Technol.* 104 (2019) <http://dx.doi.org/10.1007/s00170-019-03844-6>.
- [76] D. An, Y. Zhang, R.C. Yang, Numerical modelling of 3D concrete printing: material models, boundary conditions and failure identification, *Eng. Struct.* 299 (2024) <http://dx.doi.org/10.1016/j.engstruct.2023.117104>.
- [77] A. Suiker, Mechanical performance of wall structures in 3D printing processes: Theory, design tools and experiments, *Int. J. Mech. Sci.* 137 (2018) <http://dx.doi.org/10.1016/j.ijmecsci.2018.01.010>.
- [78] Z. Chang, H. Zhang, M. Liang, E. Schlangen, B. Šavija, Numerical simulation of elastic buckling in 3D concrete printing using the lattice model with geometric nonlinearity, *Autom. Constr.* 142 (2022) 104485, <http://dx.doi.org/10.1016/j.autcon.2022.104485>.
- [79] M. Wang, H. Zhang, Q. Hu, D. Liu, H. Lammer, Research and implementation of a non-supporting 3D printing method based on 5-axis dynamic slice algorithm, *Robot. Comput.-Integr. Manuf.* 57 (2019) <http://dx.doi.org/10.1016/j.rcim.2019.01.007>.
- [80] N. Niknafs Kermani, S.G. Advani, J. Férec, Orientation predictions of fibers within 3D printed strand in material extrusion of polymer composites, *Addit. Manuf.* 77 (2023) 103781, <http://dx.doi.org/10.1016/j.addma.2023.103781>.
- [81] Y. Wei, S. Han, S. Yu, Z. Chen, Z. Li, H. Wang, W. Cheng, M. An, Parameter impact on 3D concrete printing from single to multi-layer stacking, *Autom. Constr.* 164 (2024) <http://dx.doi.org/10.1016/j.autcon.2024.105449>.
- [82] Q. Zhan, H. Wu, L. Zhang, P. Yuan, T. Gao, 3D concrete printing with variable width filament, in: *ECAADe 2021: Towards a New, Configurable Architecture*, 2021, pp. 153–160, <http://dx.doi.org/10.52842/conf.ecaade.2021.2.153>.
- [83] B. Korte, J. Vygen, *Combinatorial Optimization: Theory and Algorithms*, Springer, Berlin, Germany, 2012, <http://dx.doi.org/10.1007/978-3-642-24488-9>.
- [84] A. Jipa, M. Bernhard, B. Dillenburger, Submillimeter formwork: 3D-printed plastic formwork for concrete elements, in: *TxA Emerging Design + Technology*, Austin, 2017, pp. 1–13.
- [85] N. Volpato, L.C. Galv textasciitilde ao, L.F. Nunes, R.I. Souza, K. Oguido, Combining heuristics for tool-path optimisation in material extrusion additive manufacturing, *J. Oper. Res. Soc.* 71 (6) (2020) 867–877, <http://dx.doi.org/10.1080/01605682.2019.1590135>.
- [86] S. Singh, A. Singh, S. Kapil, M. Das, Utilization of a TSP solver for generating non-retractable, direction favouring toolpath for additive manufacturing, *Addit. Manuf.* 59 (2022) <http://dx.doi.org/10.1016/j.addma.2022.103126>.
- [87] Y. Shinagawa, T. Kunii, Y. Kergosien, Surface coding based on morse theory, *IEEE Comput. Graph. Appl.* 11 (5) (1991) 66–78, <http://dx.doi.org/10.1109/38.90568>.
- [88] M. Hilaga, Y. Shinagawa, T. Kohmura, T.L. Kunii, Topology matching for fully automatic similarity estimation of 3D shapes, in: *Proceedings of the 28th Annual Conference on Computer Graphics and Interactive Techniques*, ACM, 2001, <http://dx.doi.org/10.1145/383259.383282>.
- [89] S. Huang, W. Xu, H. Hu, Space-filling and print path generation methods for large-area 3D concrete printing pavements, *Archit. Intell.* 2 (1) (2023) 13, <http://dx.doi.org/10.1007/s44223-023-00032-1>.
- [90] Y. Hu, T. Schneider, B. Wang, D. Zorin, D. Panozzo, Fast tetrahedral meshing in the wild, *ACM Trans. Graph.* 39 (4) (2020) <http://dx.doi.org/10.1145/3386569.3392385>.
- [91] Y. Zhi, Ovenbird, 2024, URL: <https://www.food4rhino.com/en/app/ovenbird>.
- [92] T. Teng, Y. Zhi, K.-H. Yu, S. Yang, M. Akbarzadeh, Continuous multi-filament 3D printing for tension-compression structure components, in: *Proceedings of IASS 2023 Symposium Integration of Design and Fabrication*, Melbourne, Australia, 2023, pp. 126–138.
- [93] T. Teng, Y. Zhi, M. Akbarzadeh, Functionally graded architectural materials: integrated and tailored thermal insulation through gradient multimaterial additive manufacturing for masonry architectural components, in: *Proceedings of the 44th Annual Conference of the Association for Computer-Aided Design in Architecture (ACADIA)*, Banff, Canada, 2024, pp. 1–11.
- [94] T. Teng, Y. Zhi, M. Akbarzadeh, Prototyping high-fidelity multifunctional objects using single-nozzle multi-filament additive manufacturing system with active mixing, *Mater. Des.* 249 (2025) <http://dx.doi.org/10.1016/j.matdes.2024.113479>.